J. Fluid Mech. (2009), *vol.* 633, *pp.* 191–231.
doi:10.1017/S0022112009006971 Printed in the United Kingdom

Turbulent transport mechanisms in oscillating bubble plumes

MARCO SIMIANO[1,2]†, D. LAKEHAL[3], M. LANCE[4] AND G. YADIGAROGLU[5]

[1]ETH Zurich, Laboratory of Nuclear Energy Systems, ML K 14, CH-8092 Zurich, Switzerland

[2]Paul Scherrer Institut, Thermal-Hydraulics Laboratory, CH-5232 Villigen PSI, Switzerland

[3]ETH Zurich and ASCOMP GmbH, Technoparkstrasse 1, CH-8005 Zurich, Switzerland

[4]University Claude-Bernard Lyon 1, Lyon, France

[5]ETH Zurich, WEN, Weinbergstrasse 94, CH-8006 Zurich, Switzerland

(Received 20 April 2008 and in revised form 26 January 2009)

The detailed investigation of an unstable meandering bubble plume created in a 2-m-diameter vessel with a water depth of 1.5 m is reported for void fractions up to 4 % and bubble size of the order of 2.5 mm. Simultaneous particle image velocity (PIV) measurements of bubble and liquid velocities and video recordings of the projection of the plume on two vertical perpendicular planes were produced in order to characterize the state of the plume by the location of its centreline and its equivalent diameter. The data were conditionally ensemble averaged using only PIV sets corresponding to plume states in a range as narrow as possible, separating the small-scale fluctuations of the flow from the large-scale motions, namely plume meandering and instantaneous cross-sectional area fluctuations. Meandering produces an apparent spreading of the average plume velocity and void fraction profiles that were shown to remain self-similar in the instantaneous plume cross-section. Differences between the true local time-average relative velocities and the difference of the averaged phase velocities were measured; the complex variation of the relative velocity was explained by the effects of passing vortices and by the fact that the bubbles do not reach an equilibrium velocity as they migrate radially, producing momentum exchanges between high- and low-velocity regions. Local entrainment effects decrease with larger plume diameters, contradicting the classical dependence of entrainment on the time-averaged plume diameter. Small plume diameters tend to trigger 'entrainment eddies' that promote the inward-flow motion. The global turbulent kinetic energy was found to be dominated by the vertical stresses. Conditional averages according to the plume diameter showed that the large-scale motions did not affect the instantaneous turbulent kinetic energy distribution in the plume, suggesting that large scales and small scales are not correlated. With conditional averaging, meandering was a minor effect on the global kinetic energy and the Reynolds stresses. In contrast, plume diameter fluctuations produce a substantial effect on these quantities.

† Present address: ETH Zurich, Institute of Energy Technology, Laboratory of Nuclear Energy Systems, ML K 14, CH-8092 Zurich, Switzerland. Email address for correspondence: msimiano@lke.mavt.ethz.ch

1. Introduction

1.1. *State of the art in experimental investigation of bubble plumes*

Older studies of bubble plumes (e.g. by Kobus 1968 and Milgram 1983) produced the basic understanding about their global behaviour. More recent detailed bubbly flow experiments (Hassan *et al.* 1992; Delnoj *et al.* 1999; Kubasch 2001; Rensen & Roig 2001; Simiano *et al.* 2006) were conducted with confined flows or bubble columns. Various effects including recirculation in the vessel and the presence of walls can make the plume centreline and boundaries oscillate in three dimensions. These effects can also produce large structures driving the dispersed phase. The three-dimensionality of air–water bubbly flows was revealed in various experiments; Milgram (1983), Castello-Branco & Schwerdtfeger (1994), Kuwagi & Ozoe (1999) and Johansen *et al.* (1988) discuss plume precession and swirling. The radial distributions of the void fraction and of the velocities were investigated by several authors, e.g. Tacke *et al.* (1985) and Johansen *et al.* (1988).

Turbulence in bubbly flows has been central to the research in this area. Experiments of Johansen *et al.* (1988), Gross & Kuhlman (1992) and Iguchi *et al.* (1995) revealed that turbulence is in general isotropic in the core flow, whereas anisotropy was shown to take place only near the walls by Grevet, Szekely & El-Kaddahn (1981). This was to be expected indeed, but a detailed description of the exact role of the gas phase in producing anisotropy of turbulence – and its proportions – was not given. Iguchi, Takeuchi & Morita (1991) found that the velocity fluctuations may be of the same order of magnitude as the mean velocities (100 % turbulence intensities), and follow a Gaussian distribution. In the experiments of Johansen *et al.* (1988), measured turbulent intensities were weaker axially than in the experiment of Iguchi *et al.* (1991), i.e. about 50 %, but still substantially stronger in the radial direction (>100 %) except near the free surface.

The above selected experimental findings indicate that several phenomena in this class of flows are not yet well understood. Further, the results are sometimes contradictory, in particular concerning turbulence. One key issue here is the distinction between shear-induced small-scale turbulence and large-scale transient motions inherent to the stability of the plume itself. The research in this direction has been somewhat ambiguous, notably because the separate contributions of these two phenomena to the global time-averaged characteristics of bubbly plumes have never been distinguished properly.

A fairly exhaustive literature survey on bubbly plumes can be found in Simiano (2005), and is not repeated here. Simiano *et al.* (2006) have listed the main publications.

1.2. *Scope of the work*

Most of the previously mentioned detailed experimental studies were focused on bubbly flows with a void fraction range below 0.2 %. The experiments reported in the present work cover a void fraction ranging from 0.5 % to 4 %.

In a previous publication, Simiano *et al.* (2006) presented a comprehensive investigation of the most important hydrodynamic characteristics of fairly large-scale bubble plumes. Their plumes, produced in a 2-m diameter vessel with a 0.3-m diameter circular bubble injector, exhibited the usual meandering behaviour. In addition, the shape and dimensions of the plume cross-section varied in time and the structure of the plume showed the typical unstable behaviour recently reported, for example, by Rensen & Roig (2001). As one of the goals of the Simiano *et al.* (2006) study was to determine the turbulent characteristics of the plume and study the fluctuating

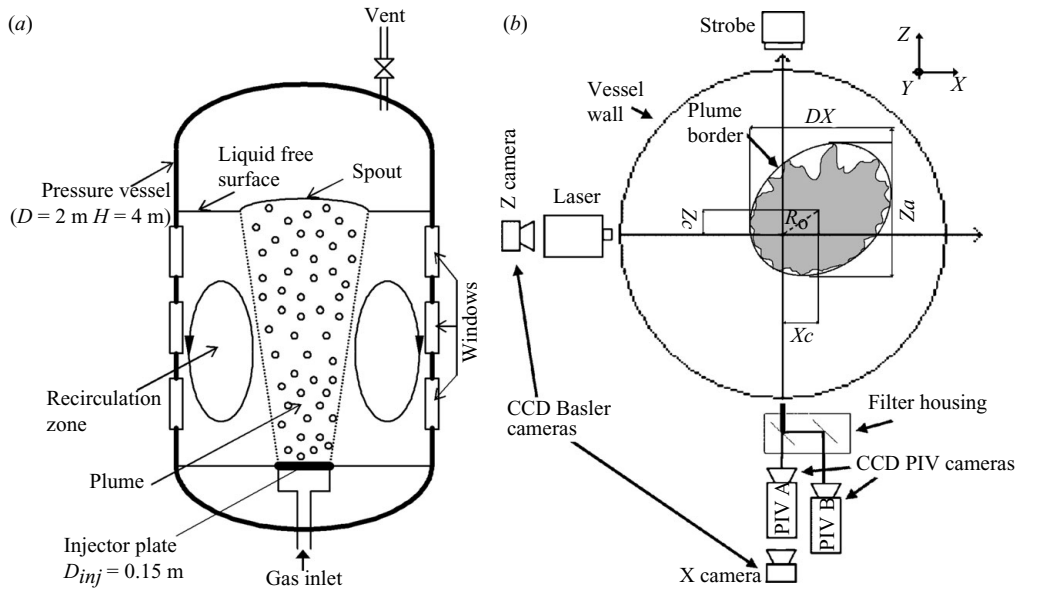

FIGURE 1. Bubble plume experiment in the LINX facility (*a*). Top view schematic of the experimental setup used to detect simultaneously the instantaneous bubble plume position and the velocity fields of the two phases (*b*).

components of the main flow variables, it became evident that the usual averages of the data (referred to here as 'global averages'), produced with an unstable plume were not at all representative of any instantaneous plume condition. The meandering and instabilities of the plume were indeed 'spreading' the profiles of the variables of interest and the local fluctuations obtained via global averaging of the data were affected by the macroscopic instabilities of the plume. It also became clear that attempts to 'stabilize' the plume were questionable and would had affected its behaviour. A much more promising way would have been to study the characteristics of the plume making use of conditional ensemble averages according to its instantaneous state.

As a single PIV camera was used in the previous measurements, the velocities of the two phases had to be recorded in separate experimental runs, not allowing the investigation of the interactions and correlations between the two phases, in particular the measurement of the true instantaneous relative velocity between the bubbles and the liquid and the computation of its mean.

In the new set of experiments reported here, the instrumentation was completed in a novel way to: (i) allow the simultaneous estimation of the two phase velocities, using two PIV cameras now, and (ii) to record and characterize the state of the plume structure simultaneously with the PIV velocity measurements.

As the plume meanders, its centreline is most of the time outside the vertical PIV plane passing through the centreline of the injector and the PIV fields capture in reality information along a 'chord' (see figure 1). The 'chordal' PIV velocity information obtained in this 'apparent diameter' is clearly of limited usefulness. In the present experiments, the position of the plume centreline and its projected diameters in two perpendicular planes were obtained by an ad-hoc two-camera video system and used to process the PIV data: conditional ensemble averages were produced according to the state of the plume, in particular the position of the plume centreline with respect to the PIV plane and an 'equivalent' plume diameter defined later. The

turbulent data processed via conditional averages showed important differences from 'globally averaged' data.

The information obtained by the classical 'global' averages with an oscillating and meandering plume contains the traditional information on, e.g. the average spreading of the plume. Global averaging certainly does not produce statistical information on local phase velocities and their fluctuations, Reynolds stress terms, etc., related to the instantaneous plume characteristics such as the diameter and position of the plume. Although the traditional data are useful for the development and validation of plumespreading models and time-average Reynolds averaged Navier–Stokes (RANS) computations, there are not adequate for the validation of more advanced computational fluid dynamics (CFD) techniques such as LES that are capable of producing the time–dependent history of the plume. In particular, if closure laws (e.g. for bubble lift forces) are validated using globally time-averaged data and time-average RANS results, there is no assurance that these laws will perform adequately in predicting time-dependent results in, for example, LES computations. These considerations have driven the second campaign of experiments whose results are presented in this paper.

Following a brief description of the experimental setup, of the instrumentation, of the global behaviour of the plume, and of some plume characteristics, the PIV data are presented and analysed in the following two main parts of the paper. In Part A we exploit mainly the data collected at low elevations near the injector. In this region there is practically no plume meandering and instabilities and the fairly stable bubble plume structure allows the simple use of the classical time averages, or *global averages* for the characterization of important quantities of the flow. Important findings in this part are made regarding the relative velocity of the bubbles with respect to the liquid.

As already noted, the bubble plume exhibited a strong instability of its entire structure, which, at higher elevations, made the classical global time averaging inadequate for the study of this flow. Thus, in Part B, we resorted to the novel concept of conditional averaging, performed according to the state of the bubble plume, namely the position of its centreline and its equivalent diameter. Conditional averaging allowed separation of the effect of the large-scale motion and instabilities of the plume from the effects of the small-scale turbulent fluctuations inside the plume and produced observations that would have not been possible otherwise.

We, in particular, show that the large-scale motions have no effect on the turbulent transport mechanisms. The classical long-time global averages are indeed not adequate for the study of inherently unstable two-phase flows, and lead to misleading evaluation of the turbulent transport mechanisms.

2. Experimental setup

The bubble plume was produced in the LINX facility, a metallic vessel filled with demineralized water (figure 1) (Simiano *et al.* 2006). The vessel is 2 m in diameter and 3.4 m in height. Twelve glass windows allow visual, photographic and PIV observations from outside.

As the state of the plume right above the injector will affect transport phenomena downstream, a careful control of the initial conditions is needed in performing such experiments. The bubble plume was produced by a sophisticated injection device, consisting of 140 hollow needles with an outside diameter of 2 mm and inside diameter of 1 mm, uniformly distributed, in a 10-mm-pitch square array, over a circular

horizontal plate with a diameter $D_{inj} = 150\,\text{mm}$ (while the previous experiments of Simiano *et al.* (2006) were conducted with a 300 mm injector). The needles were fed from the laboratory air supply through 0.8-m-long, 0.3-mm-diameter capillary tubes that throttle the gas flow and produce uniform gas distribution, bubble generation and a narrow bubble size distribution (Simiano *et al.* 2006). The bubbles, at about 150 mm elevation, had an ellipsoidal shape with a shape factor $e \approx 0.5$ and an equivalent (Sauter) diameter of 2.5 mm. Rising single bubbles of this size are well known to follow oscillatory, spiralling or zigzagging paths.

The coordinate system used is the following: the vertical coordinate is denoted as elevation or Y and is always measured from the top of the injector needles; the horizontal ones are denoted as X and Z when no axial symmetry is assumed and r otherwise and are measured from the axis of the injector (figure 1). The vertical and horizontal velocity components are denoted as v and u, respectively.

As reported by Simiano *et al.* (2006) the PIV measurements were of lesser quality on the side of the plume away from the laser source; for this reason, only data from the region closer to the laser source are used and plotted.

The plumes studied here have complex instantaneous structures, where the velocity and void fraction profile widths certainly do not 'coincide'. We refer to 'bubble plume diameter' as the diameter of the region occupied by bubbles.

The double-tip optical probe system used for void fraction estimation is described by Simiano (2005).

2.1. *Simultaneous two-phase PIV technique*

Simultaneous liquid- and gas-phase velocity measurements are made possible by seeding the liquid with fluorescent particles and observing the laser light emitted by the seeds as well as the light reflected by the bubble surfaces (Simiano 2005). The simultaneous two-phase PIV (STP-PIV) system used is commercial Dantec equipment with a dual Yag laser (532 nm, 100 mJ) and two 1×1 kpixel (Kodak ES 1.0) cameras with one-byte grey level. The recording system separates and samples simultaneously the signals from the two phases: the first camera, with an orange filter, detects the fluorescent water seeds and the second camera, with a green filter corresponding to that of the laser wavelength, detects only the reflections from the bubbles in the same observation window.

The laser produced a 2-mm-thick vertical light sheet placed at the centre of the injector. The seeds used were 40 μm diameter poly(methyl methacrylate) (PMMA) fluorescent particles (Rhodamine B as fluorescent substance), with a density of $1.19\,\text{g}\,\text{cm}^{-3}$, and a refractive index of 1.48. Uniform seeding was not a trivial issue; it was realized by injecting the seeding particles along a line below the laser sheet, just below the injector needles, using three ad-hoc loops, equipped with membrane pumps delivering a few deciliters per hour. Seeded water was forced through several needle injectors: five, equally spaced, 1-mm-inner-diameter needles, one central 1-mm-inner-diameter needle and twenty, again equally spaced, 0.2-mm-inner-diameter needles. The three loops, individually controlled by valves, allowed particle distribution and concentration regulation. PIV measurements performed just above the bubble injector, during and after membrane pump operation, did not show any differences proving the negligible effect of the seeded water flow.

The plume was observed at three different elevations using the three superimposed LINX windows (figure 1). For each investigation, three series of images were acquired; one long-time acquisition of 4000 pairs of images for each phase at 0.5 Hz (about 133-min measurements), and two short-time acquisitions of 2000 pairs of images at

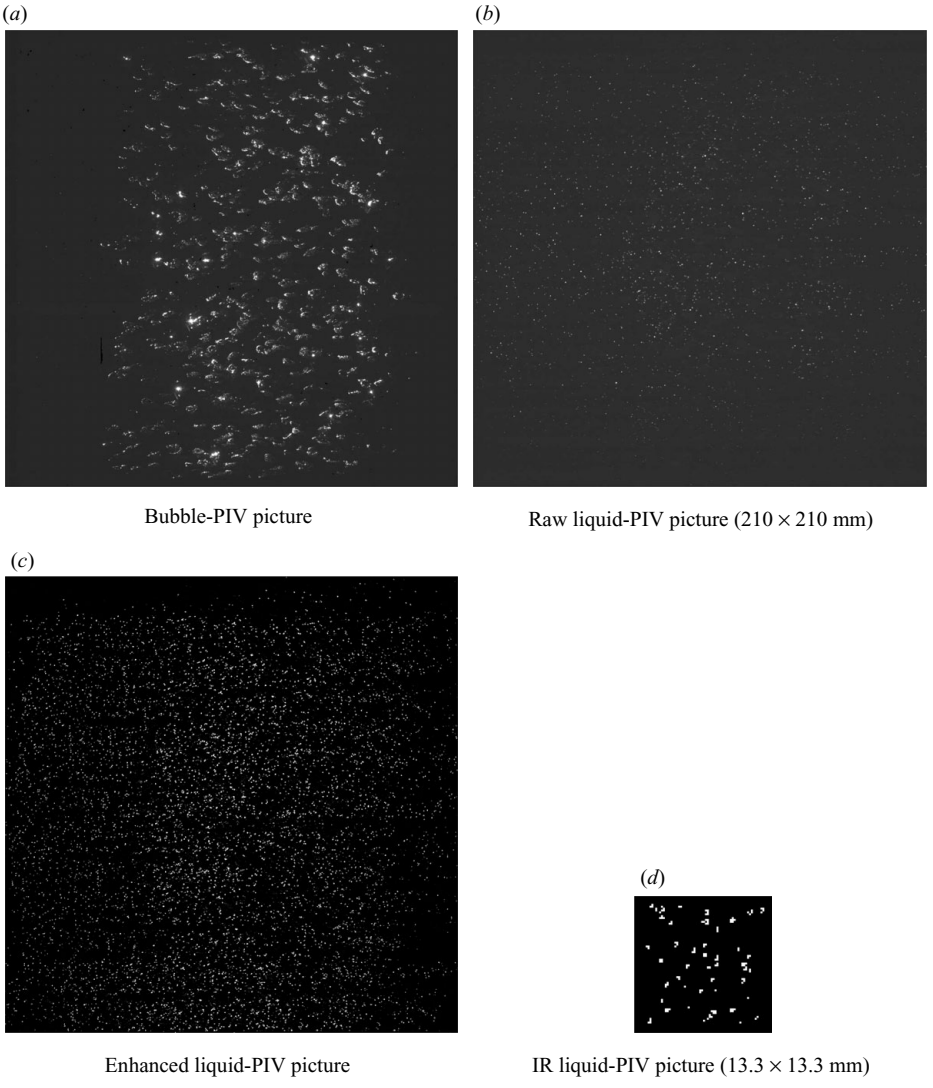

FIGURE 2. Single-shot, bubble and liquid PIV pictures acquired simultaneously for a gas flow rate of 7.5 normal litres per minute ($NL\,min^{-1}$) at and elevation ranging from 260 to 470 mm.

15 Hz (more than 2 min). The delay between two PIV pulses varied, according to the velocity to be measured, between 5 and 7 ms. Longer PIV pulse delays improve the accuracy of the cross-correlation by increasing the spatial displacement of the particles but decrease the frequency response of the signal (Simiano 2005).

The common PIV window, used for both phases, had a field of view of about 210×210 mm with a resolution of 207 μm $pixel^{-1}$; each velocity vector was calculated over an interrogation region (IR) of (64×64) pixels (about (13.3×13.3) mm) with 50 % overlapping. The total vector field consisted of 30 columns by 30 rows of vectors placed at the centre of their IRs. Examples of PIV pictures are shown in figure 2(a) for the bubbles and in figure 2(b–d) for the liquid phase.

The raw liquid-PIV picture, shown in figure 2(b), presented a low image contrast and particles poorly visible by eye. To enhance the image and consequently the

quality of the cross-correlation the background was removed from the raw images by a thresholding method and the grey-level values of the particle pixels were increased by a linear transformation. The processed image is shown in figure 2(*c*), where the contrast is increased and the particles appear much brighter. Following an optimization study the threshold value was chosen as the mean pixel grey level, obtained by averaging several consecutive pictures. The linear-transformation imposed the saturation value (255 for the 8-bit camera) to the pixels having the peak values. The seeds were resolved as 3–4 pixels, as shown in figure 2(*d*).

2.2. *Physical interpretation of the PIV measurements*

Generally any true instantaneous local phase-velocity component φ_j^{true} can be decomposed as

$$\varphi_j^{true} = \varphi_j + \varphi_j^{unres}, \tag{2.1}$$

where φ_j is the experimentally resolved velocity obtained with the spatial and time averaging inherent to PIV, and φ_j^{unres} is the unresolved velocity component that was filtered out by the intrinsic PIV filtering, as discussed summarily here and in more detail by Simiano *et al.* (2006). The time delay between the two PIV pulses and the finite size of the IR introduce the time filtering and the space averaging of the measured velocities, respectively.

With our laser pulse delays of 5–7 ms (corresponding to frequencies of 200 and 140 Hz, respectively), according to the time response of an integral time filter (Simiano 2005; Simiano *et al.* 2006), a 100 Hz signal (typical frequency of turbulent eddy production in the bubble wake, estimated also as the ratio between the relative velocity (o)10^{-1} m s^{-1} and the bubble diameter (o)10^{-3} m) will be attenuated to about 0.64 of its true amplitude for the 5 ms delay and to about 0.37 for the 7 ms delay.

Regarding space filtering, the phase velocities are averaged over the volume defined by the IR of (13.3 × 13.3) mm) and the laser beam thickness of 2 mm as width. The size of the IR plays the same role in space filtering as the width of the pulse in time filtering. Consequently, velocity fluctuations associated with small scales of a few millimetres, will be significantly attenuated by the space filter. The attenuations to 0.64 and 0.37 of the true signal, estimated above for the time filtering, correspond now to fluctuating velocities with spatial scales on the order of 27–20 mm (corresponding, e.g. to eddies of that size).

It is evident that the high frequencies and the effect of small scales will be attenuated and the measured kinetic energy will be lower due to both the time and space filtering effects. The spectra of the turbulent kinetic energy are, however, strongly weaker at high frequencies and the loss of turbulent kinetic energy in our estimation will not be very large. A quantitative estimate of the effect of the attenuation of the high frequencies requires knowledge of the full spectrum, something that PIV data cannot deliver. One should note, however, that although the high-frequency space and time fluctuations are not resolved, their effects on the well-resolved larger spatial time scales are present in the data. Our turbulence data measured with the PIV system should be compared to fully resolved data computed by say direct numerical simulation (DNS) or large-eddy simulation (LES) only after similar filtering.

The filtering effect inherent to the PIV measurements should also be considered in relation to the physical interpretation of the measured average phase velocity data. First, we should recall that the PIV window (13.3 mm) is several times larger than the bubble diameter (2.5 mm) and that, at the void fractions of our experiments, there are typically not more than two or three bubbles present in the IR. As the

PIV camera detects the reflections from the bubbles, the measured gas velocities will correspond to the average bubble velocity in the IR at any time. Regarding the measured average liquid velocities that come from the seeding particles present only in the liquid, it is clear that the PIV data correspond to the average or bulk velocity of the liquid contained in the IR. As there is a liquid velocity gradient near the bubble, the measured liquid velocity may depend on the size of the IR, but for bubbles significantly smaller than the IR, the measurement should approach that of the true bulk velocity.

The last item to discuss is the physical interpretation of the measured instantaneous relative velocities between bubbles and liquid. The definition of the relative velocity of a single bubble rising in liquid is simple if the liquid velocity is measured at 'infinity'. The definition of the appropriate liquid velocity for swarms of bubbles must necessarily be made with respect to a liquid bulk velocity measured in the space between bubbles (the liquid velocity is equal to the bubble velocity at the surface of the bubble and there is no 'velocity at infinity' in this case). Formally, the average relative velocity should be the ensemble average over all possible bubble configurations in the IR; our statistical averages with a few bubbles only in the IR should approach this ideal. Additional remarks regarding the relative velocity measurements are made in the Appendix.

2.3. *Video recording system in two perpendicular directions*

Besides the STP-PIV system, an image acquisition system (IAS) recorded images (projections) of the bubble plume in two vertical planes from two perpendicular directions. This system consisted of two CCD Basler digital video cameras with a resolution of (640×480) pixels and 1-byte grey level. Figure 1(b) shows the layout of the STP-PIV and IAS systems.

A strobe light synchronized with the IAS illuminated the plume just after the PIV shots. An example of a couple of IAS images is shown in figure 3. The pictures were processed to remove light gradients and possible saturated/burned pixels. Despite this, the two pictures show some differences due to either the optical filter applied to the lens of the Z camera to protect its chip from any reflected laser light, or the strobe light position that made the lightening non-uniform.

2.4. *Plume behaviour and test matrix*

The plume at the beginning has a diameter close to that of the injector D_{inj}. Downstream, in the region between two and three injector diameters it contracts to about 70 % of D_{inj}. The plume is relatively stable near the injector. Further downstream it exhibits, however, an unstable behaviour, consisting mainly of a meandering around its axis and plume cross-sectional area fluctuations, both increasing with distance from the injector.

The test matrix, table 1, was set up to study the influence of the gas flow rate on the important hydrodynamic characteristics of the bubble plume. The gas flow rates were chosen to obtain a void fraction range of about $0.2\,\% < \alpha < 4\,\%$.

Table 1 presents also the time-averaged void fraction at the injector centreline α_0 and the time- and cross-sectional-average void fraction α_s obtained from measurements over a radius of $r = 0$ to 150 mm assuming azimuthal symmetry. The water level in the tank was 1.5 m above the top of the injector needles.

Test	I_1	I_2	I_3	I_4
Air mass flow rate ($\mathrm{nl\,min^{-1}}$)	1.9	3.5	7.5	15
Air mass flux over injector area ($\mathrm{g\,m^{-2}s^{-1}}$)	2.31	4.57	9.15	18.3
α_0 at $Y = 156$ mm (%)	0.43	0.92	2.08	4.07
α_s at $Y = 156$ mm (%)	0.21	0.52	0.74	1.45

TABLE 1. Test matrix of the set of experiments.

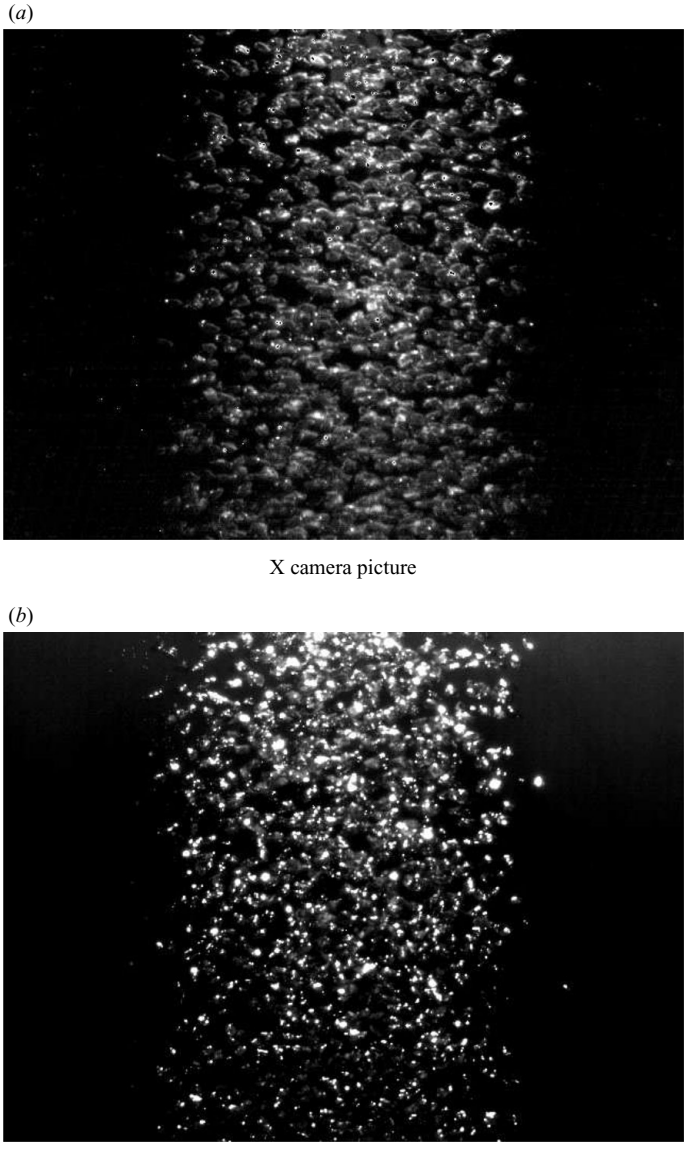

FIGURE 3. A pair of CCD Basler camera pictures, taken from perpendicular directions, for a gas flow rate of 7.5 NL $\mathrm{min^{-1}}$ covering the elevation range from 160 to 350 mm.

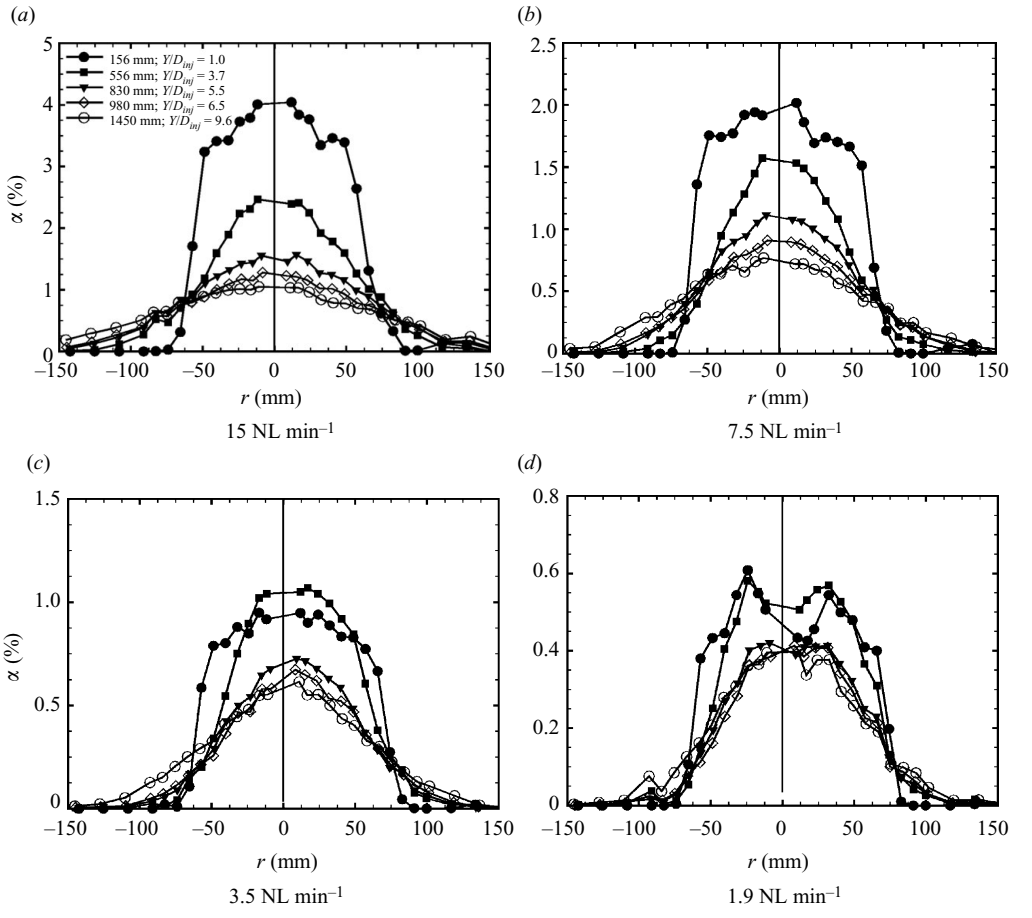

FIGURE 4. Time-averaged void fraction distributions at different elevations for all air flow rates.

3. Void fraction measurements

The local time-averaged void fraction was obtained from the optical probe signal (Cartellier 1990; Cartellier & Achard 1991; Wu & Ishii 1999):

$$\alpha = \sum_i T_{G_i}/T, \tag{3.1}$$

where T_{G_i} are the gas presence times and T is the total duration of the measurement. Radial void fraction scans were conducted at selected elevations; these consisted of 30 point measurements; each point was scanned for 15 min for the two higher air flow rates (15 and 7.5 NL min^{-1}). For the low flow rates, due to the low bubble frequency, the signal was acquired for 30 min. The time-averaged void fraction profiles plotted at several elevations are shown in figure 4.

The profiles show the expected decrease of the centreline peak void fraction and a broadening of the distribution with elevation, which are more pronounced at the higher flow rates of 15 and 7.5 NL min^{-1}. However, in the region close to the injector, α decreases with Y also because of bubble acceleration. The broadening of

the void fraction profiles of the plume, for 15 and 7.5 NL min^{-1}, is perceptible only downstream of $Y/D_{inj} > 1$. Close to the injector ($Y/D_{inj} \leqslant 1$) the profiles have very steep edges.

For the lower flow rates of 3.5 and 1.9 NL min^{-1}, the broadening is visible only at the third level (830 mm elevation; $Y/D_{inj} = 5.5$), while below this elevation, the profile shrinks, presenting a higher peak at 3.5 NL min^{-1} (figure 4*c*), or remains roughly constant at 1.9 NL min^{-1} (figure 4*d*). Such a contraction was also visually observed at the higher flow rates, but at lower elevations where no sensor was present. The broadening seems to be somewhat delayed at low flow rates where the profiles kept their sharp edges up to $Y \approx 6D_{inj}$ from the injector.

Although the definition of the void fraction given above implies sufficiently long-time averaging, dynamic information can nevertheless be obtained by means of a frequency analysis if the void fraction data are averaged only over short time periods. This approach revealed a dominant frequency corresponding exactly to the plume precession period (about 100 s) that was also made evident by the analysis of the video images of the plume reported in § 4.2 below. More details of the void fraction spectrum can be found in Simiano (2005).

4. Global dynamics of the three-dimensional bubble plume structure

The new two-directional IAS allowed much better estimations of the overall plume structure, and in particular of its equivalent diameter, than those made in the earlier work of Simiano *et al.* (2006) where the shape of the plume was obtained from the PIV images of the bubbles. As the plume centreline is not in general on the PIV plane, these 'apparent' cross-sections were in reality chordal cuts of the plume, as shown in figure 1. The IAS allows determination of the real plume projections on two perpendicular planes, from which the plume position and equivalent diameter can be better (but clearly not perfectly) estimated. Figure 1(*b*) defines the variables DX, DZ, X_c and Z_c, denoting the projected plume diameters and centreline positions, respectively. These quantities were estimated using a Matlab routine which detects the contours of the plume on the images; details can be found in Simiano (2005).

The oscillatory behaviour of the plume, observed visually, consists mainly of an apparently stochastic motion of the plume around its axis, with plume width and horizontal cross-section fluctuations increasing with distance from the injector. The inner part of the plume evolves quite non-homogeneously, reflecting the presence of a wide spectrum of gaseous inclusions (clusters of bubbles) and turbulence structures. The horizontal cross-section does not remain circular, but fluctuates, shrinks and stretches in all directions.

The three-dimensional plume structure dynamics can be analysed by looking at the consecutive instantaneous plume edge reconstructions reported in figure 5. The projections extracted from the video pictures are plotted in the YZ and YX planes of figure 5; the solid red lines indicate the centrelines of these projections. The three-dimensional images of the plume volume were obtained by assuming, for the sake of visualization only, an instantaneous ellipsoidal horizontal cross-section with the axes of the ellipse along X and Z. The reconstructed three-dimensional volume of the plume shows waves propagating upwards (the vertical arrows in figure 5), as well as the instantaneous displacement of the plume centreline from that of the injector.

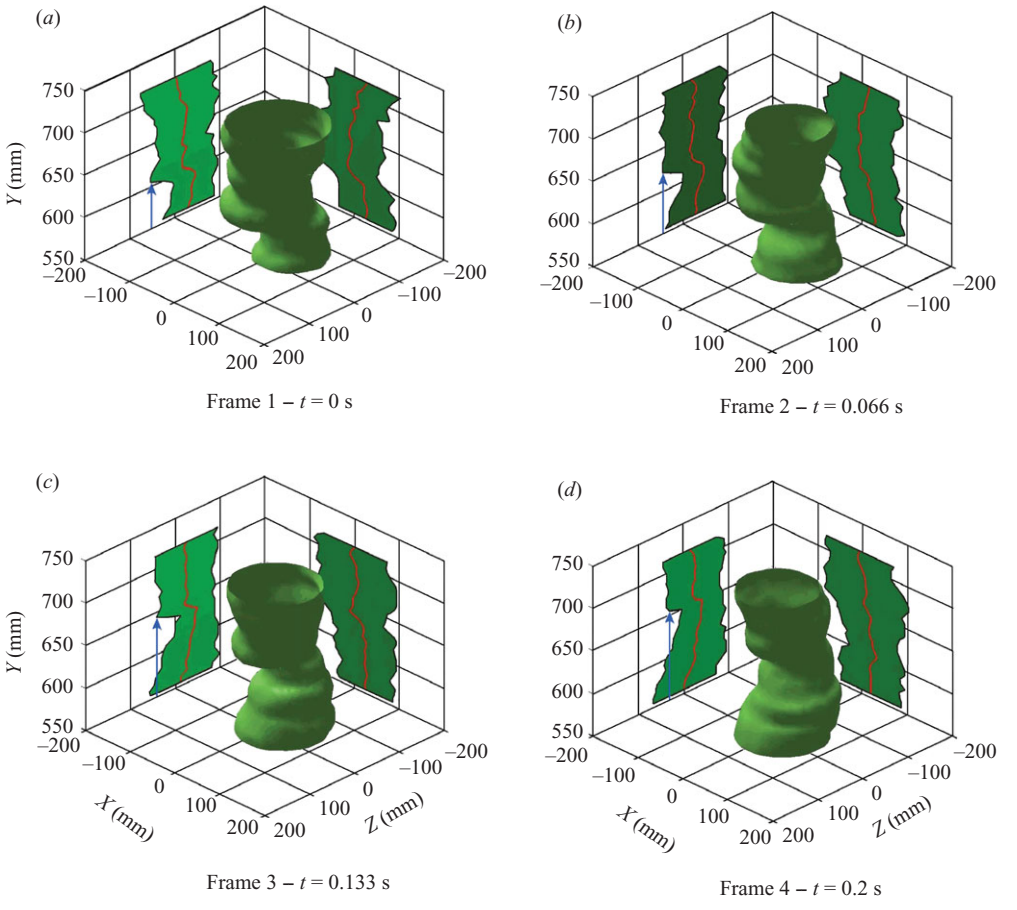

FIGURE 5. Time sequence of three-dimensional plume reconstructions produced using information obtained with the two-directional video recording system; gas injection rate of 15 NL min^{-1}.

4.1. *Plume spreading*

Since only two perpendicular vertical projections of the structure were recorded† an equivalent plume diameter D_e was defined as (see figure 1):

$$D_e = (DX + DZ)/2. \tag{4.1}$$

Previous investigations of bubble plumes (Kobus 1968; Milgram 1983; Fannelop, Hirschberg & Kuffer 1991) revealed an increase of the width of the time-averaged liquid velocity profiles with elevation. Kobus (1968), based on a Gaussian description of the mean liquid velocity profile, introduced the rate of spread b as

$$\overline{v}_L = \overline{v}_{L0} \cdot \mathrm{e}^{\frac{-r^2}{b^2}}. \tag{4.2}$$

In figure 6 the normalized averaged spreading of the bubble-plume core D_e/D_{inj} (continuous lines) is compared with the normalized rate of spread $2b/D_{inj}$ (symbols)

† A horizontal PIV image of the plume would have revealed much better its cross-sectional shape but was technically not possible.

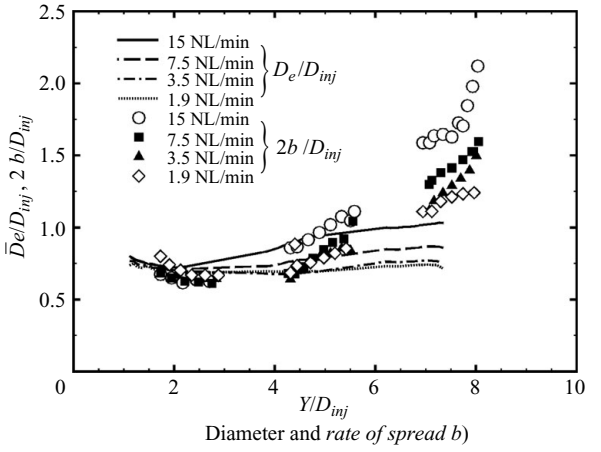

FIGURE 6. Time-average bubble plume diameters D_e and the *rate of spread* b of the mean liquid velocity profile normalized with the injector size D_{inj} at the four gas injection rates.

obtained by fitting the mean liquid velocity profiles with (4.2) for all gas flow rates. At any instant, there is little plume diameter spreading in the experiment, although the measured time-averaged liquid velocity (and also void fraction) profiles show much greater broadening at higher elevations. The comparison clearly shows that in agreement with the earlier qualitative observations of Simiano *et al.* (2006) based on PIV images, it is the meandering or the oscillation of the axis of the plume that makes the time-averaged profiles significantly flatter and broader at higher elevations rather than a diffusive systematic spreading of the plume core.

The role of the meandering or of the large-scale motion in general and their impact on the time-averaged fields is an important issue, addressed in detail in Part B of this work.

4.2. *Plume meandering*

Spectral analysis of the long-time recording of the axial position of the plume structure confirmed the presence of main modes, remaining constant with elevation, while increasing linearly with gas flow rate (Simiano *et al.* 2006) in agreement with (Milgram 1983) and (Rensen & Roig 2001).

Due to the large period of plume meandering (of a few minutes, as reported by Simiano *et al.* (2006) and Simiano (2005)), both long-time low-frequency and short-time high-frequency series of images were acquired as noted in § 2.1. The long-time investigation revealed that the position of the plume centre for both projections presented a probability density function (pdf) symmetric with respect to its mean central position, as shown in figure 7(*a*).

Furthermore, the instantaneous centreline of the bubble plume position r_C, obtained by the 'fast', short-time investigations (figure 7*b*), defined as:

$$r_C = \sqrt{{X_C}^2 + {Z_C}^2}, \tag{4.3}$$

where X_C and Z_C are the displacements of the plume centre in the two observation frames, shows very slow plume meandering with a period of the order of the minute.

The bubble plume structure instability in terms of meandering of the plume centreline (RMS of r_C) and variation of its diameter (RMS of D_e) presents a visible evolution with elevation, as reported in figure 8. This instability is rather weak close

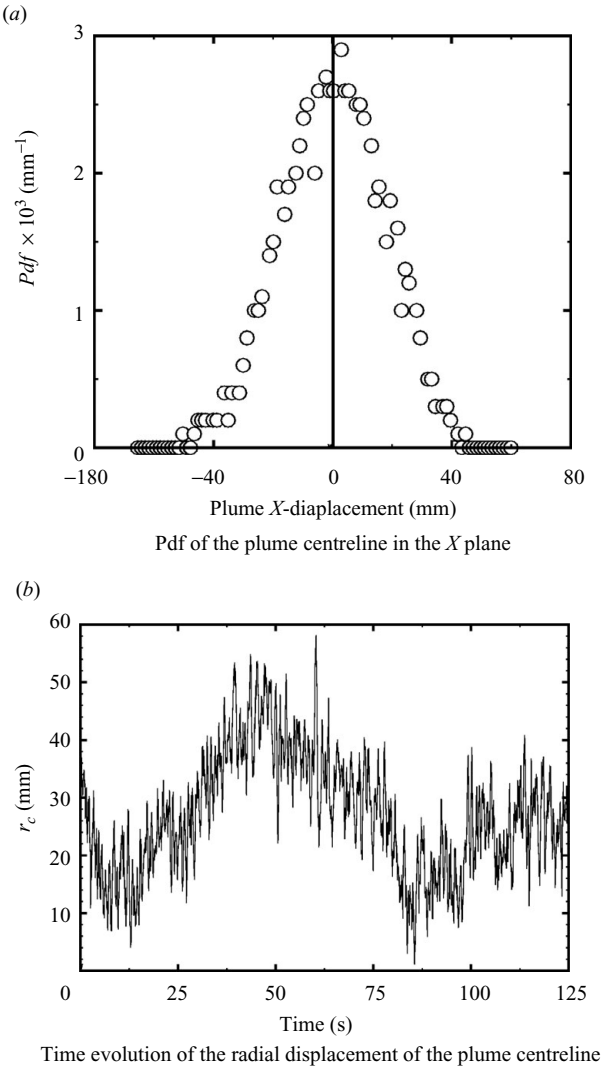

FIGURE 7. Probability density function of the x displacement of the bubble plume structure obtained from the 0.5 Hz measurements (a). Time evolution of the radial position of the bubble plume structure recorded at 15 Hz (b). Observation for the gas flow rate of 15 NL min^{-1} at the 739.5 mm elevation.

to the injector, it consistently grows up at about $Y/D_{inj} = 4 - 5$, to reach saturation further downstream. This justifies the use of classical time averages close to the injector (presented in Part A) and of conditional averages (Part B) further downstream to investigate the role of the plume instability on the turbulent transport mechanisms.

Part A

Measurements made near the injector are discussed in this part of the paper. As plume meandering was negligible at the low elevations investigated here, classical time averaging of the data was sufficient. The PIV data, analysed without considering the meandering effects are termed here *global* averages, in contrast to the conditional

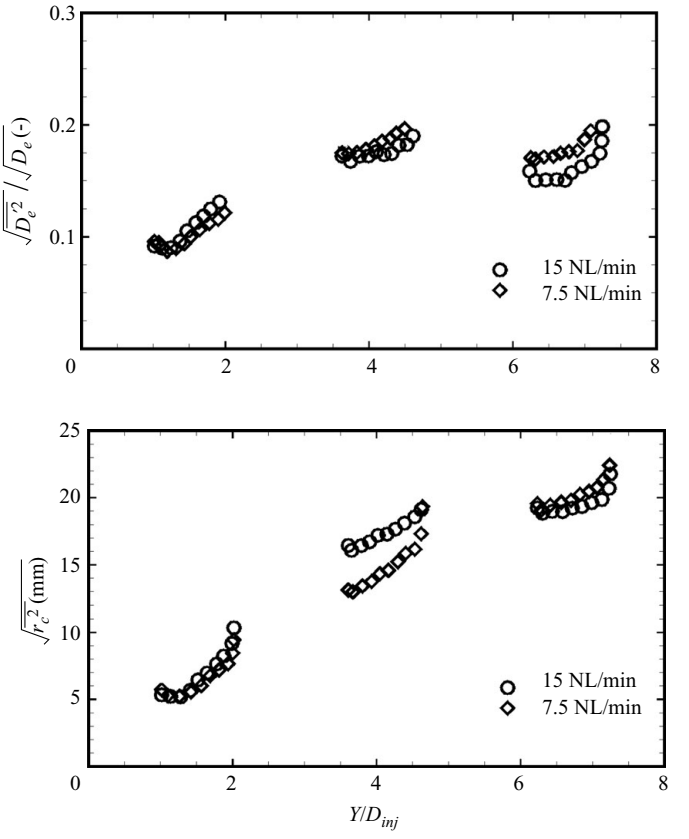

FIGURE 8. Evolution along the elevation of the root mean square of the bubble plume normalized diameter and its centreline radial position at the 7.5 and 15 NL min^{-1} flow rates.

averages discussed in Part B of this paper. Most of the results presented were obtained at the highest gas flow rate of 15 NL min^{-1}, unless otherwise noted.

5. Simultaneous two-phase flow PIV results

As the liquid- and gas-phase measurements were acquired simultaneously, the averaged relative velocity is the 'true' mean of the instantaneous difference between the phase velocities within the limits imposed by the intrinsic PIV filtering discussed earlier. The need for simultaneous two-phase measurements is in fact crucial because the bubble and liquid velocities are strongly correlated. The derivation of the average relative velocity from the averaged phase velocities is incorrect, as shown here.

Figure 9 compares the true mean relative velocity with the difference of the mean phase velocities. The two measurements coincide at the plume centre, but exhibit significant differences near the edge. The reason for this difference is rigorously explained in the Appendix. Direct measurements of relative velocity obviously require the presence of a bubble in the PIV interrogation region. This restriction does not hold when measuring the average liquid velocity profile; that measurement depends only on sufficient seeding of the fluid. As the liquid velocities tend to be higher in the presence of the bubbles, this leads to a bias towards lower averaged liquid velocities. Consequently, the true relative velocity becomes lower than the difference of the

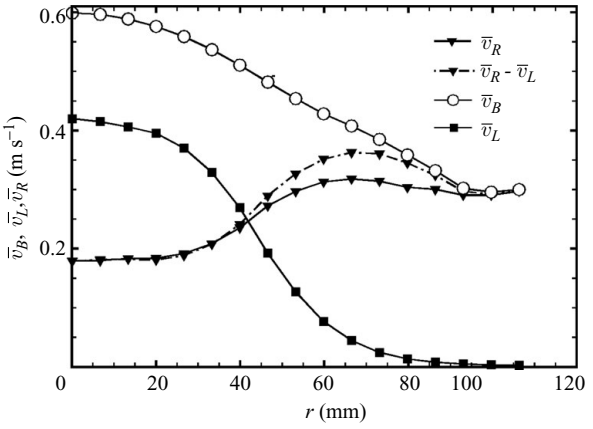

FIGURE 9. Comparison between the mean relative velocity $\overline{v}_R$ and the difference between the mean phase averages $\overline{v}_B$ and $\overline{v}_L$, measured at the 15 NL min^{-1} flow rate and at the 438 mm elevation.

averages. This difference vanishes close to the plume centre where the void fraction is higher and therefore there is a higher probability of simultaneity between presence of a bubble in the IR and velocity estimation.

5.1. *Time averaged bubble, liquid and relative velocities close to the injector*

The mean bubble, liquid and relative velocities are plotted in figure 10 for several elevations close to the injector. The bubble velocities present flat profiles very close to the injector, with centreline values increasing with elevation. The profiles evolve slowly with elevation in a rather uniform way. In the zones near the plume edge (highlighted in grey), some points are averaged over only a few velocity vectors; this explains some of the scatter at $r > 90$ mm.

The liquid velocity field shown in figure 10(b) presents instead much steeper gradients. The profiles are quite flat and broad at the 259–272 mm elevations, featuring sharp edges at the periphery. At higher elevations, the profiles evolve substantially reaching a higher centreline velocity (up to 0.4 m s^{-1}) and smoother edges. The evolution of the liquid velocity profiles also reflects the contraction of the plume just above the injection discussed previously.

The time-averaged relative velocities compared in figure 10(c) present more complex radial profiles and trends with elevation. The relative velocity increases with elevation for $r > 35$ mm, while it decreases otherwise. The radial variation of the relative velocity is not monotonic. These evolutions will be discussed now on the basis of several sets of observations.

First, we examine the vorticity of the liquid phase defined as:

$$\overline{\omega}_L = \frac{\partial \overline{v}_L}{\partial r} - \frac{\partial \overline{u}_L}{\partial y}. \tag{5.1}$$

Very close to the needles, the liquid profiles shown in figure 10(b) present sharp edges at around $r = 60$ mm, which correspond to the peaks of the liquid vorticity shown in figure 10(d) since $|\partial \overline{v}_L/\partial r|$ is much higher than $|\partial \overline{u}_L/\partial y|$ (see Simiano (2005) and § 8.1 for the horizontal liquid velocity profiles). The high-liquid vorticity is associated with vortices which intermittently are formed at the injector edge and travel upward while being quickly deformed because of the bubbles and turbulence. In figure 11,

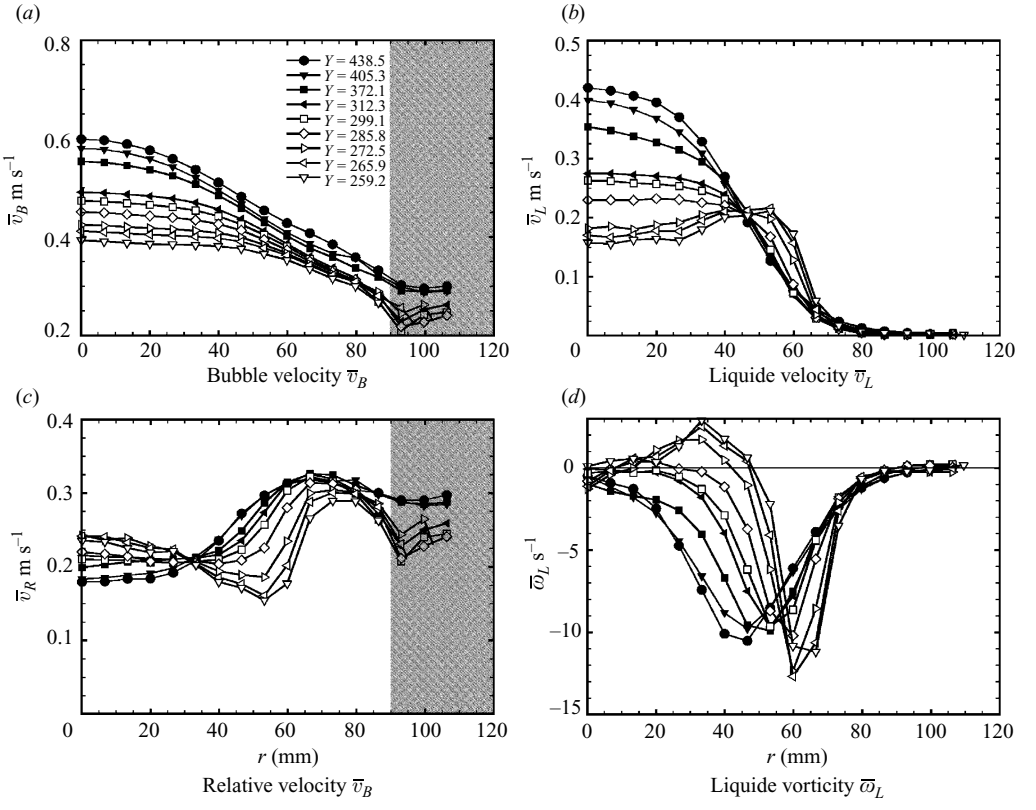

FIGURE 10. Average bubble, liquid and relative velocities and liquid vorticity at the injection rate of 15 NL min^{-1} and at various elevations. The grey colour highlights the radial locations, near the plume edge, where the mean bubble and relative velocity profiles are averaged over only a few velocity vectors due to the much lower local void fraction at the plume periphery.

selected contour plots of the instantaneous vorticity fluctuations ($\omega'_L = \omega_L - \overline{\omega}_L$) are reported. Vortices, corresponding to high-vorticity zones, can be observed in consecutive snapshots as they move upwards. Their lifetime appears to be short due to the presence of the bubbles which deform and destroy these structures downstream. These vortices interact with the bubbles, drifting them also laterally by the action of the lift force (which depends on $\overline{\omega}_L$). Their effect disappears when the vortices themselves are dissipated at higher elevations.

A further manifestation of the intermittent 'bubble-vortex interaction', which occurs at the plume periphery ($r = 60$ mm), just above the bubble injector, appears in the local pdf of the normalized vertical relative velocity reported in figure 12. At the 265 mm elevation ($Y/D_{inj} \approx 1.8$) (figure 12*a*), the pdf distribution presents two peaks associated with two 'typical' velocities which correspond to the instantaneous velocities of bubbles interacting with large vortices (low relative velocities) and to the instantaneous velocities of bubbles rising without 'vortex-bubble interaction'. Moreover, cases of relatively immobile bubbles can also be observed ($v_R/\overline{v}_R = 0$) which have, as shown in figure 12, a very low but finite probability; this phenomenon is, however, less noticeable at higher elevation. The two peaks of the pdf distribution are still present at the 312 mm elevation ($Y/D_{inj} \approx 2$) (figure 12*b*), while they have already merged at $Y = 438$ mm (figure 12*c*), in the region where the averaged relative velocity has

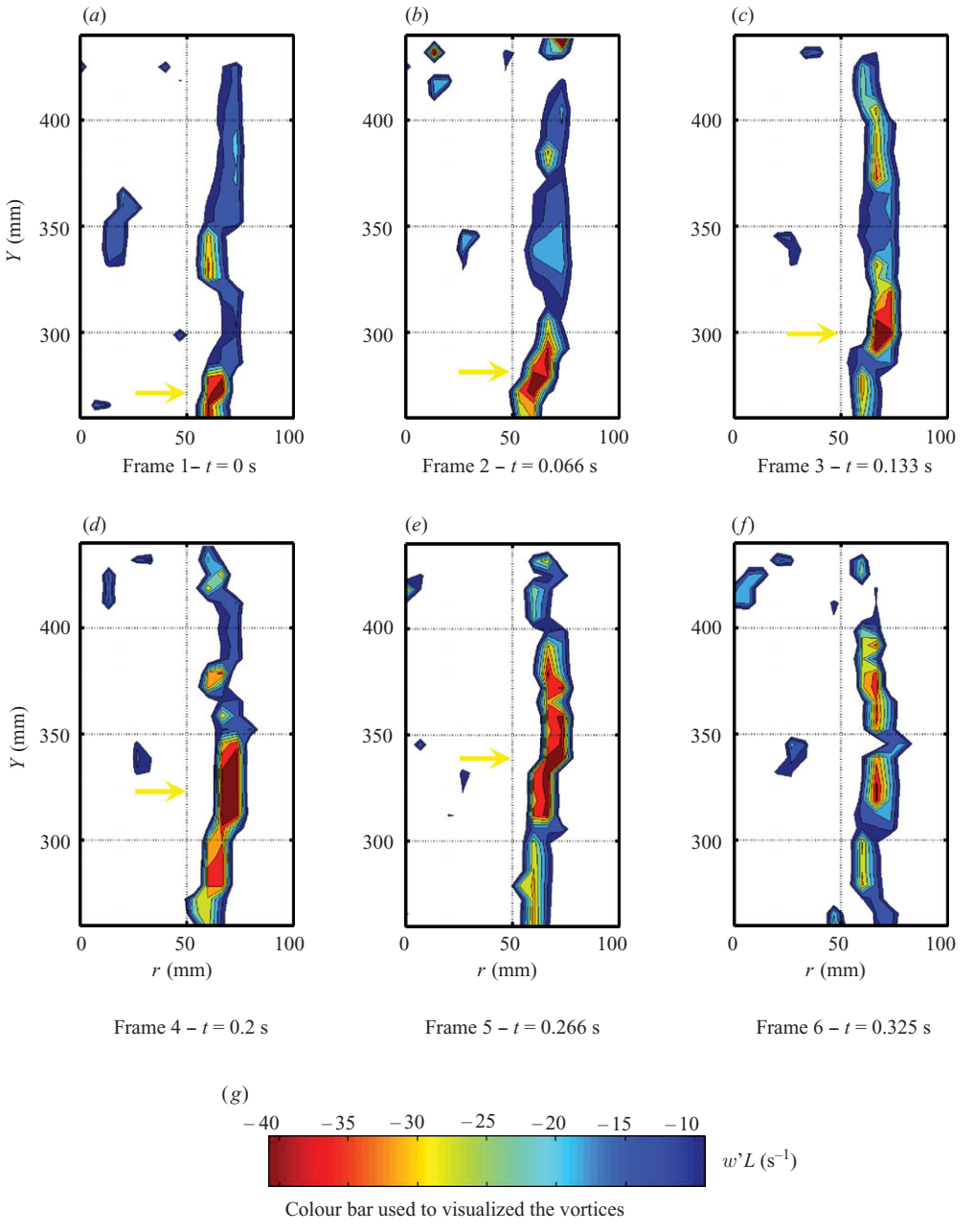

FIGURE 11. Maps of the fluctuation of the vorticity $\omega'_L = \omega_L - \overline{\omega}_L$. Gas flow rate of 15 NL min^{-1}.

recovered an almost monotonic trend and no longer changes much with elevation (figure 10*c*).

The bubble-vortex interaction was already studied in the past (Rightley & Lasheras 2000; Mazzitelli & Lohse 2003). Mazzitelli & Lohse (2003) who numerically investigated the motion and the action of microbubbles in homogenous and isotropic

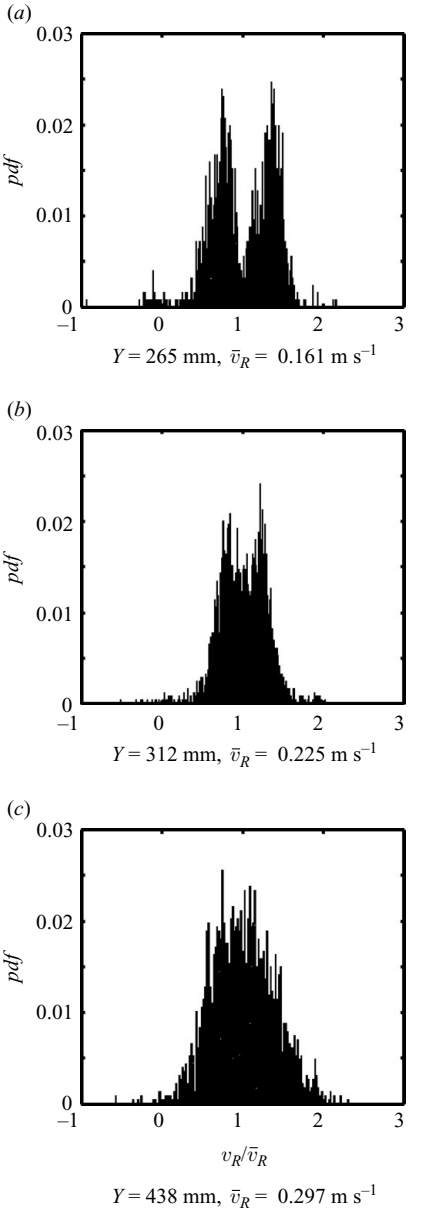

FIGURE 12. Probability density function of the normalized relative velocity at $r = 60$ mm and for three different elevations at the injection rate of 15 NL min^{-1}.

turbulence, found the bubbles accumulating in vortices, preferably on the side with downward velocity, under the action of the lift force. This action resulted in a reduced bubble rise velocity since the lift force featured a downwards component. A direct comparison with the findings of Mazzitelli & Lohse (2003) is, however, quite difficult due to the very different parameters of their flow.

Experimental investigations of similar bubbly flows (Rensen, Luther & Lohse 2005; van Den Berg *et al.* 2006) have also shown the accumulation of the bubbles on the

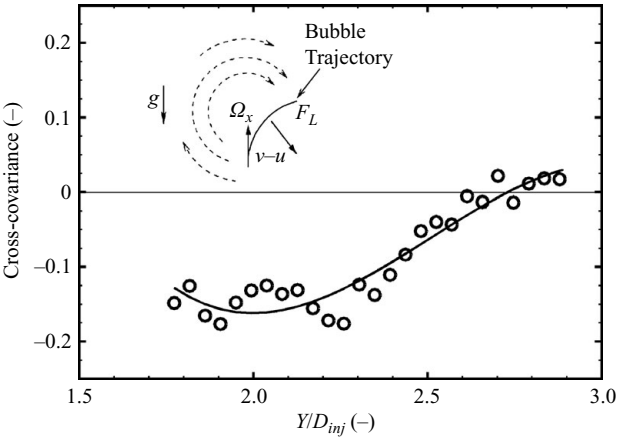

FIGURE 13. Cross-covariance of the vorticity and relative velocity fluctuations, as function of the elevation, at $r = 60$ mm and for the injection rate of 15 NL min^{-1}.

downward-velocity side of the vortices (created by the negative lift force acting downwards).

The proposed bubble-vortex interactions, as an explanatory mechanism for the vertical evolution of the relative velocity at the periphery of the bubble plume, can be further justified by estimating the cross-covariance (normalized cross-correlation) of the vorticity and the relative velocity fluctuations at several elevations, figure 13. The cross-covariance presents fairly large negative values, due to the anti-correlation of the two quantities. As for the bimodal pdf of the relative velocity of figure 12, the effect disappears higher up where the vortices have already lost most of their energy or have already been dissipated.

The multitude of evidence given above supports the thesis that the shape of the relative velocity profile and its downward evolution near the injector can be explained by the effect of vortices created near the injector and vanishing as they travel downstream.

Above the $Y \approx 400$ mm elevation ($Y/D_{inj} > 2.6$), the relative velocity has already developed (figure 10*c*) and presents a consistent, nearly monotonic radial evolution, with lower values at the plume centre and peaking at the plume edge. This variation cannot be explained by the known influence of the radial variation of the void fraction on the drag and the relative velocity. The relationship between dispersed-phase fraction and relative velocity was studied extensively in the past (Zuber & Findley 1965; Ishii & Zuber 1979). The motion of a given particle is affected by the presence of the neighbouring particles, which is translated into an increase of the drag. For bubbles in the distorted-particle regime, Ishii & Zuber (1979) proposed

$$V_R = V_{R\infty}(1-\alpha)^{0.75}, \tag{5.2}$$

where $V_{R\infty}$ is the terminal rise velocity for a single bubble. Equation 5.2 applied in the small void fraction range encountered in our bubble plume (say 0 to 4 %), justifies a relative velocity change smaller than 3 %. The more recent measurements of Zenit, Koch & Sangani (2001) suggest a stronger dependence of the relative velocity on void fraction, leading perhaps to differences up to 7 %. These are still too small to fully explain the radial and axial variations of the relative velocity measured in our experiments that reached up to 80 % (figure 10*c*).

The radial evolution of the relative velocity above the 400 mm elevation can be explained by: (i) the radial motion of the bubbles, combined with (ii) their slow response time. Due to their helicoidal motion and mutual interactions, the bubbles never reach their terminal velocity while moving through a strong liquid radial velocity gradient. This is supported by the larger relaxation time of the bubble τ_b, the time needed for a bubble to adjust itself to the liquid velocity, compared to the fluid-element deformation time τ_k, $\tau_b/\tau_k \approx 30$ (Hinze 1959; van Wijngaarden 1998). A bubble rising near the centre of the plume, in equilibrium with the high plume-core velocity and ejected outwards into the low-liquid-velocity region will transport its higher relative velocity and vice versa for bubbles migrating from the periphery towards the core of the plume. In essence, any time a bubble moves radially it simply takes some time to adjust to the new local velocity. On the average, this momentum exchange due to bubble migration is reflected in the shape of the averaged relative velocity of figure 10(*c*).

5.2. *Globally time-averaged turbulence properties*

Figure 14 shows the normal and the shear Reynolds stresses, $\overline{u'_L u'_L}$, $\overline{v'_L v'_L}$, $\overline{u'_L v'_L}$ at different elevations, starting with the one closest to the injector, at 266 mm, and moving further up to 438 mm. Similar measurements were also presented by Simiano *et al.* (2006); however, in the experiments reported here the stresses have been evaluated at much lower elevations. This has revealed an interesting evolution of peak values, which present a clear correlation with the average liquid velocity gradients discussed in the context of figure 10(*b*). The stress distributions show two peaks marked as 1, 2 at the two lowest elevations, at about $r = 65$ mm from the injector centreline. These peaks correspond to the sharp edge of the liquid velocity profile shown in figure 10(*b*) at the same elevations. At higher elevations (285–312 mm), the peaks marked as 3, 4, 5 shift to shorter radial distances, with smaller or comparable stress values, again in accordance with the liquid velocity slopes presented in figure 10(*b*). Moving away from the injector (372–438 mm elevations), the peaks marked as 6, 7, 8 move towards the centre at about $r = 45$ mm and show a significant increase in intensity. This shift is another manifestation of the bubble plume contraction discussed in the context of figure 6.

The axial stresses of figure 14(*b*) are more important than the radial components. Two distinct regions can be identified: below and above the $Y = 300$ mm elevation ($Y/D_{inj} = 2$). In the lower region, the distribution of the stresses is self-similar, with peaks located at $r = 60$ mm. The stresses increase with elevation in the second region ($Y/D_{inj} > 2$), with peak locations shifting towards the plume centre. The behaviour of these stresses reflects the pulsating motion of the plume in the flow direction, as discussed previously. Form earlier plume-surface reconstruction results (figure 5), we can infer that plume contraction is associated with strong liquid velocity gradients in both the axial and radial directions. Thus, the creation and destruction of the resulting turbulent stresses, or, more precisely, the exchange mechanisms between these stresses and the mean flow are controlled by this contraction-acceleration mechanism. The correlation between these stresses and the liquid velocity gradient ($\partial \overline{v}_L/\partial r$), and thus the vorticity $\overline{\omega}_L$ is well illustrated in the figures. In this flow region, the v'_L fluctuations take energy from the mean flow in the radial direction, which explains why low-stress zones (peaks 1, 2, 3, 4) correspond to high velocity-gradient zones in figure 10(*d*), and vice versa.

Comparing the two normal stresses $\overline{u'_L u'_L}$ and $\overline{v'_L v'_L}$ plotted in figure 14 clearly reveals that turbulence is strongly anisotropic. In the well-developed flow regions,

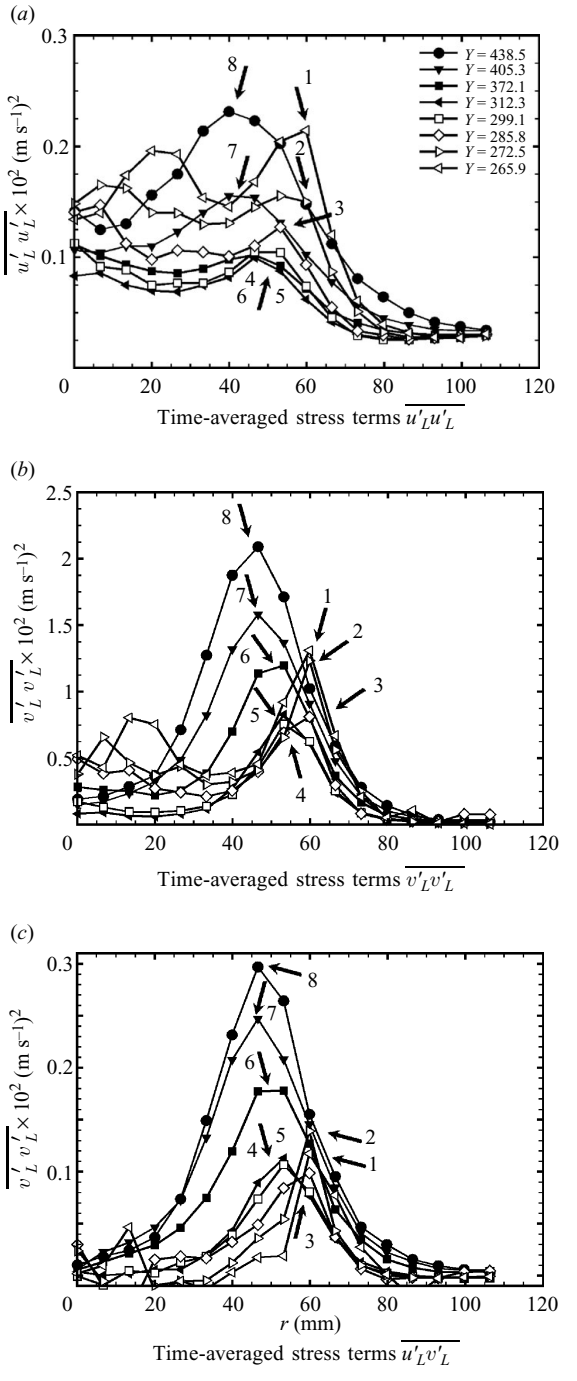

FIGURE 14. Globally averaged Reynolds stress profiles of the liquid phase at the gas injection rate of 15 NL min^{-1}, at various elevations. The numbers and the arrows indicate the peak positions of the stresses at different elevations.

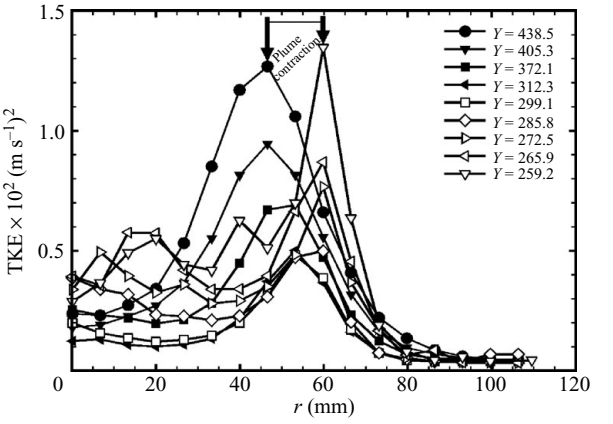

FIGURE 15. TKE at several elevations, for the 15 NL min^{-1} flow rate.

turbulence along the flow direction is sometimes one order of magnitude larger. Very close to the injector, where the liquid has not yet accelerated, the anisotropy ratio $\overline{v'_L v'_L}/\overline{u'_L u'_L}$ reduces to about 5.

The shear stress distributions shown in figure 14(c) can also be seen to correlate with the liquid-velocity gradients, and thus with vorticity $\overline{\omega}_L$ since $|\partial\overline{v}_L/\partial r| \gg |\partial\overline{u}_L/\partial y|$. This is a consistent result in view of the previous discussion of liquid velocity and vorticity distributions. This signature of the energy-redistribution mechanism cannot be explained within the context of isotropic turbulence modelling, where

$$\overline{v'_L v'_L} = 2/3K - \nu_t \frac{\partial \overline{v_L}}{\partial y}, \tag{5.3}$$

with ν_t, the eddy viscosity and K, the 'exact' definition of the turbulent kinetic energy. Indeed, the expression above does not show explicitly the contribution of $\partial\overline{v_L}/\partial r$, in contrast to what is manifestly suggested by figures 10(b,d), but that of $\partial\overline{v_L}/\partial y$ only. The same is true for the $\overline{u'_L u'_L}$ components, which is shown to be driven by the combined action of $\partial\overline{u_L}/\partial y$ and $\partial\overline{u_L}/\partial r$, which appears in its equivalent expression to (5.3):

$$\overline{u'_L u'_L} = 2/3K - \nu_t \frac{\partial \overline{u_L}}{\partial r}. \tag{5.4}$$

The normal stresses, $\overline{u'_L u'_L}$ and $\overline{v'_L v'_L}$, are indeed generated by the combined action of $\partial\overline{u_L}/\partial r$ and $\partial\overline{u_L}/\partial y$, and $\partial\overline{v_L}/\partial r$ and $\partial\overline{v_L}/\partial y$, respectively, in total odds with the isotropic concept reflected by (5.3) and (5.4).

The combined effect of the normal stresses can be better quantified by looking at the turbulent kinetic energy (TKE), defined as:

$$TKE \approx \frac{1}{2}(2 \cdot \overline{u'_L u'_L} + \overline{v'_L v'_L}), \tag{5.5}$$

where the azimuthal fluctuating component, which could not be measured by the PIV system, was considered, as proposed by Iguchi *et al.* (1995), by assuming an azimuthal stress equal to the radial one.

The dominant behaviour of $\overline{v'_L v'_L}$ is clearly revealed by figure 15, comparing the TKE at different elevations. The peaks of the TKE located at $r < 50$ mm correspond to the contraction zone discussed previously. The vorticity distribution (figure 10c)

has an obvious relationship with TKE: the peak locations, in particular, coincide at each elevation.

In summary, it appears that the production of the normal stresses is closely related to the contraction of the plume, and that it coincides with vortices created at the edge of the injector and then convected upwards. The region where these interactions occur is at the plume outer periphery, but with a distinct evolution: in the lowest region ($Y/D_{inj} < 2$) where the vortices do not oscillate much as the plume is still stable, the stresses behave almost self-similarly, whereas, in the upper part, the pulsating motion of the plume is more pronounced, drifting more vigorously the vortices, translating into a quasi-linear increase of the normal stresses with height.

Part B

In this part, the data obtained at higher elevations will be examined. As the plume was clearly unstable and meandering at these elevations, conditional averaging techniques will be used. Again, the data presented were obtained at the highest gas flow rate of 15 NL min^{-1}, unless otherwise noted.

6. Flow decomposition and conditional averages

6.1. *Triple flow decomposition*

Generally, in the classical Hussain and Reynolds flow decomposition, an instantaneous measured quantity can be expressed as,

$$\varphi_j = \langle \varphi_j \rangle + \varphi'_j, \tag{6.1}$$

where $\langle \varphi_j \rangle$ is the generic ensemble average and φ'_j is the 'randomly' fluctuating part (φ'_j can also be regarded as that part of the instantaneous quantity φ_j which is completely filtered out by the ensemble averaging operator $\langle\,\rangle$). Under the ergodic hypothesis, ensemble averages would coincide with time averages. However, in case of persistent large-scale motion in a turbulent flow such as large passing waves, dominant vortices or, as in our case, bubble plume meandering, the fluctuating term φ'_j of (6.1), includes also contributions from the large-scale motions and their interaction with the mean flow. These are phenomenologically different from small-scale (turbulent) fluctuations and therefore have to be treated separately.

Thus, starting from (6.1), it is possible to proceed to a further detailed decomposition separating the effects of the large-scale (LS) motions. The instantaneous, measured quantity (velocity) can be decomposed now as

$$\varphi_j = \langle \varphi_j \rangle + \underbrace{\varphi_j^{sub} + \varphi_j^{*} + \tilde{\varphi}_j}_{\varphi'_j}, \tag{6.2}$$

where the fluctuating term φ'_j has been further decomposed into three parts: φ_j^{sub} representing the sub-scale fluctuation, $\tilde{\varphi}_j$ the proper LS motion (meandering velocity) and φ_j^{*}, which instead arises in the local measurements from the effects of the LS motion on the flow (i.e. the displacement of the bubble plume structure from its central position due to meandering). Using simple long-time averages only the mean $\langle \varphi_j \rangle$ and the sum of the three fluctuating terms φ'_j are usually evaluated, making it impossible to distinguish between the different contributions to the fluctuations as highlighted by means of the following simple example.

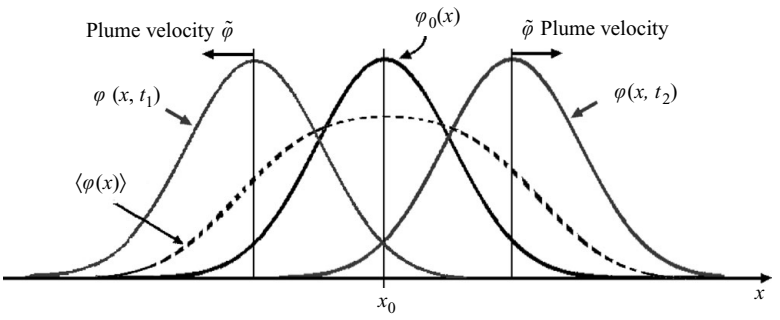

FIGURE 16. Schematic illustration of the global-time and conditional averaged velocity profiles for a simple meandering "plume".

Consider a vertical velocity profile $\varphi_0(x)$, function of the horizontal coordinate x, with maximum at x_0, as shown in figure 16. Assume now that, due to the presence of a LS motion, the velocity profile translates without deforming in the x direction, around the centre x_0, as schematically shown in figure 16. Assume that this motion is a periodic cycle with frequency f and amplitude $\tilde{\varphi}$. The instantaneous measurements of the velocity $\varphi(x,t)$ will reveal a fluctuation induced by the transverse motion of the velocity profile. If the velocity field is sampled at a given point x for time much longer than $1/f$, the time-averaged $\langle\varphi(x,t)\rangle$ will be considerably different from the instantaneous $\varphi_0(x)$ (see figure 16). The instantaneous measured velocity $\varphi(x,t)$ can therefore be decomposed into two parts: The ensemble averaged velocity $\langle\varphi(x,t)\rangle$, and the meandering-induced apparent fluctuation $\varphi^*(x,t)$. The last term does not contribute to the average velocity field by definition ($\langle\varphi^*(x,t)\rangle = 0$), while it does contribute to the mean kinetic energy $\langle\varphi(x,t)\,\varphi(x,t)\rangle$, which now includes the portion due to the mean flow $\langle\varphi(x,t)\rangle^2$ plus the portion induced by meandering $\langle\varphi^*(x,t)\rangle^2$. Assuming the energy associated with the superimposed oscillation to be negligible ($\tilde{\varphi}^2 \ll \varphi_0(x)^2$), the integral of the mean kinetic energy across the x direction of the flow with and without the LS meandering must be equal and can be written as,

$$\int_{-\infty}^{+\infty} \langle\varphi(x,t)\,\varphi(x,t)\rangle \mathrm{d}x = \underbrace{\int_{-\infty}^{+\infty} \langle\varphi_0(x)\rangle^2 \mathrm{d}x}_{\textit{Steady state}} \approx \underbrace{\int_{-\infty}^{+\infty} (\langle\varphi(x,t)\rangle^2 + \langle\varphi^*(x,t)\rangle^2)\,\mathrm{d}x}_{\textit{Non-steady state}}. \tag{6.3}$$

It is clear from (6.3) that meandering has induced an apparent fluctuating flow $\varphi^*(x,t)$, containing some of the mean kinetic energy. We call such a fluctuation 'meandering-induced apparent fluctuation'. If a 'selective sampling' of the velocity field is performed only when the vertical profile has its maximum at $x = x_0$, or at any other x, (further on this is defined as conditional average according to a specific condition k) , the ensemble average of those selected samples will be equal to the initial instantaneous velocity profile $\langle\varphi(x,t)|_k,\rangle = \varphi_0(x)$. The notation $\langle\,\rangle|_k$ refers to the particular ensemble (i.e. conditional) average estimated over samples satisfying the condition k. The mean kinetic energy (neglecting the meandering energy as $\tilde{\varphi} \ll \varphi_0$) would again be equal to the kinetic energy of the mean flow, i.e. $\langle\varphi(x,t)|_k\ \varphi(x,t)|_k\rangle = \langle\varphi(x,t)|_k\rangle^2 = (\varphi_0(x))^2$.

In other words, the use of 'selective samplings' (conditional averages) allows reconstruction of the instantaneous profile, filtering out the effect of the apparent fluctuation induced by large-scale meandering.

6.2. *Conditional averages*

Due to the limitations of the conventional time averages discussed above, conditional averages are proposed for analysing the effect of LS motion on the mean and the fluctuating flow. Designating as $\varphi_j|_k$ the instantaneous velocity φ_j when a generic condition k occurs

$$\varphi_j|_k = \langle\varphi_j\rangle|_k + \underbrace{\varphi_j^{sub}|_k + \tilde{\varphi}_j|_k}_{\varphi'_j|_k}, \tag{6.4}$$

where the flow consists of a meandering velocity $\tilde{\varphi}_j|_k$ and a contribution associated with the smaller scales (sub-scale) of the flow $\varphi_j^{sub}|_k$ in addition to the mean part $\langle\varphi_j\rangle|_k$. This conditional average filters out the large-scale-motion-induced apparent fluctuation (φ_j^* in (6.2)) while the fluctuating term $\varphi'_j|_k$ still includes the velocity $\tilde{\varphi}_j|_k$, proper to the LS motion.

In this work, the PIV observations were made in a horizontal layer that had a height equal to that of the PIV window; consequentially it is considered reasonable to describe bubble plume meandering as a motion of the plume in the horizontal plane. In accordance with this assumption, $\tilde{\varphi}_j$ in (6.2) and $\tilde{\varphi}_j|_k$ in (6.4) are equal to zero for the vertical direction since the plume meandering does not have a vertical velocity component.

In terms of mean kinetic energy, (6.2) leads to,

$$\langle\varphi_j\ \varphi_j\rangle = \langle\varphi_j\rangle^2 + \underbrace{\langle\varphi_j^*\ \varphi_j^*\rangle + \langle\varphi_j^{sub}\ \varphi_j^{sub}\rangle + \langle\tilde{\varphi}_j\ \tilde{\varphi}_j\rangle}_{\langle TKE\rangle}, \tag{6.5}$$

where, in the time-average sense, the mean kinetic energy $\langle\varphi_j\ \varphi_j\rangle$ contains $\langle\varphi_j\rangle^2$ due to the mean motion, $\langle\varphi_j^*\ \varphi_j^*\rangle$ induced by the plume displacement due to the presence of LS meandering, $\langle\varphi_j^{sub}\ \varphi_j^{sub}\rangle$ the small-scale turbulence contribution, and finally the energetic contribution of meandering, $\langle\tilde{\varphi}_j\ \tilde{\varphi}_j\rangle$, which is usually negligible compared to the other terms as the meandering velocities are very low. An estimate of the meandering velocity obtained from figure 7(*b*) results indeed in values of the order of the mm s^{-1}. Cross-stress contributions such as $\langle\tilde{\varphi}_j\ \varphi_j^{sub}\rangle$ vanish if one assumes that LS events in this flow do not correlate with the smaller scales as discussed in § 7.1.

With conditional averaging, (6.4) leads to the following decomposition of the mean kinetic energy

$$\langle\varphi_j\ \varphi_j\rangle|_k = \langle\varphi_j\rangle|_k{}^2 + \underbrace{\langle\varphi_j^{sub}\ \varphi_j^{sub}\rangle|_k + \langle\tilde{\varphi}_j\ \tilde{\varphi}_j\rangle|_k}_{\langle TKE\rangle|_k}, \tag{6.6}$$

including the usually small or negligible term $\langle\tilde{\varphi}_j\ \tilde{\varphi}_j\rangle|_k$. Thus, conditional averaging has eliminated the meandering-induced-apparent fluctuations and the conditional average of the turbulent kinetic energy $\langle TKE\rangle|_k$ carries now only the information about the smaller sub-scale motion.

6.3. *Definition of conditional and global time averages*

Assuming that M samples are collected in a given time interval, the ensemble (long-time) averaged velocity $\langle\varphi_j\rangle$ and the associated stresses $\langle\varphi'_j\ \varphi'_i\rangle$ contain all measured, both large- and sub-scale induced fluctuations. If a set of S samples out of the M ($S \leqslant M$) is selected according to certain conditions, such as the instantaneous plume centreline position and/or bubble plume diameter, the conditional average $\langle\varphi_j\rangle|_k$ and the conditional average stress terms $\langle\varphi'_j\ \varphi'_i\rangle|_k$ can be computed using only the samples satisfying the conditions.

If one were interested in the sub-scale fluctuations and their variation according to the instantaneous macroscopic state of the plume, the conditional averaging conditions would have included all the parameters describing that state: e.g. position and vector velocity of the centreline, cross-sectional shape, dimensions, etc. Such ideal conditional averaging is practically very difficult to reach. Short of performing such ideal treatment of the data, the conditional averages performed in the following sections are based only on plume centreline position and diameter.

7. Conditional averages according to the plume-centreline position

Conditional averages are performed in this section regardless of the plume diameter. The effect of plume diameter is studied in § 8. The plume centreline is an average over the height of the PIV window of 210 mm.

Conditional averages, according to the position of the bubble plume only, were computed as follows: The total set of samples $M = 4000$ vector fields obtained at 0.5 Hz, was divided into groups $(S_1, S_2, \ldots, S_N)$ according to the displacement of their plume centreline from the injector axis in the horizontal plane (conditions $k_1, k_2, \ldots, k_N$). The conditional average velocity field $\langle \varphi_j \rangle|_{k_n}$ consisted of the ensemble average of all vector velocity fields (of group S_n) acquired when the instantaneous plume centreline position was within a circle of radius *Delta*, centred at position P_n.

The effect of the radius *Delta* on the first and second moments of the vertical liquid velocity is shown in figure 17. *Delta* represents the resolution of the proposed method in detecting a specific condition k and should be small. On the other hand, *Delta* has to be large enough to provide an acceptable number of samples for statistically reliable conditional averages. $Delta = 5$ mm was chosen as a compromise, but also because equal to the RMS of the centreline radial bubble plume position (r_C) at very low elevation (figure 8 bottom) where the plume was very stable. Thus $Delta = 5$ mm can be considered as an asymptotic intrinsic limiting value.

7.1. *Interaction between large and small scales*

The non-correlation between large scales and turbulence sub-scales is a prerequisite for performing the triple-flow decomposition à la Hussein and Reynolds (§ 6.1) used here. In the present context, where meandering and/or diameter pulsations are motions identified as large and coherent, their non-correlation with the turbulent sub-scales would have involved the determination of the autocorrelation factor based on $\tilde{\varphi}_j$ and ${\varphi_j}^{sub}$, but this is obviously illusory, since there is no way of measuring these two quantities instantaneously and obtaining $\langle \tilde{\varphi}_j \ {\varphi_j}^{sub} \rangle$. We clarified the issue by segregating various repeatable events and comparing their average energy or enstrophy. The conditional average defined for the purpose of segregating scales is based on the centreline position of the plume lying within the circle of radius $Delta = 5$ mm, centred at the nine locations shown in figure 18, namely on the injector centreline and at eight positions 45° apart on a circle of 10 mm radius, centred on the injector centreline. Note that under conditions k_2 and k_4, for example, the centre of the *Delta* circle is out of the PIV plane, while for k_3 and k_5 the centre of the *Delta* circle is on the PIV plane but away from the injector centreline (an 'in-laser-sheet displacement' of 20 mm).

Conditional averages of the turbulent kinetic energy $\langle TKE \rangle|_k$ are plotted for the selected conditions $(k_{1\ldots9})$ in figure 18(*a*), which shows a $\pm$20–30 % scatter of the $\langle TKE \rangle|_k$ values. Perfect symmetry is, however, noted to exist between conditions k_2 and k_4 and conditions k_7 and k_8, as the corresponding $\langle TKE \rangle|_k$ overlap very closely

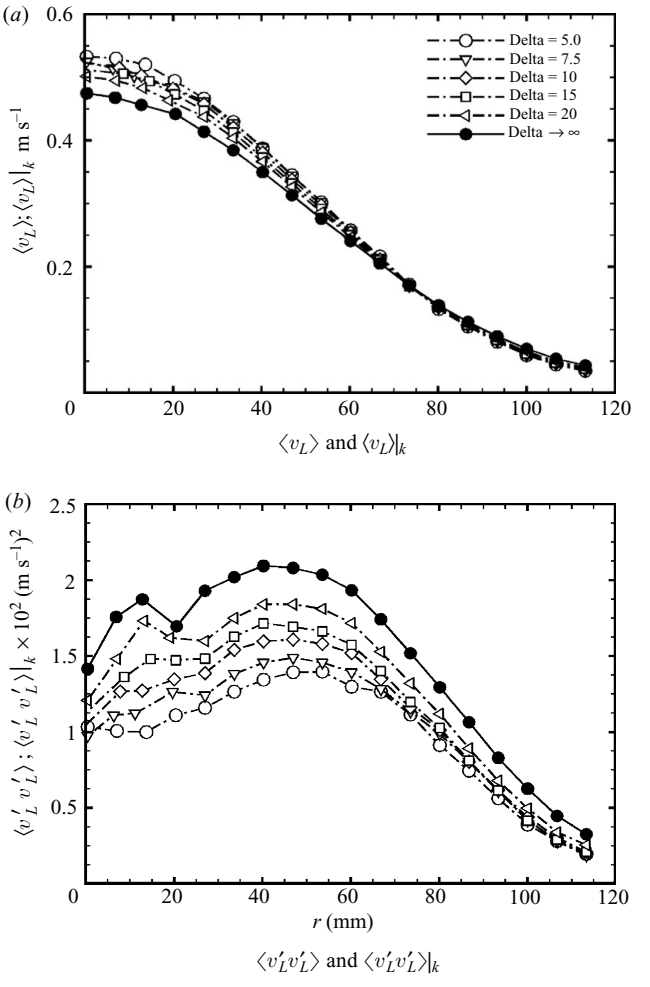

FIGURE 17. Effect of *Delta* on the conditional averages of the velocity and of the normal vertical stress for the liquid phase at the gas flow rate of 15 NL min^{-1}, at the 720 mm elevation. These conditional averages were computed for *Delta* centred on the injector centreline.

in figures 18(b,e). Figures 18(c,d) reveal a horizontal shift of the profiles which is about equal to the distance between points k_3–k_5 and k_6–k_7, respectively. If the PIV observations were 'Lagrangian' and made by following with the observation area the centre of the plume, good overlap would have been achieved for all the conditions $k_{1,\ldots,9}$.

An important finding, illustrated by figure 18, is the fact that meandering is not affecting the small-scale events, consistent with our proposed decomposition. The distributions of the turbulent kinetic energy, including both the pulsation-induced local shear and the bubble induced part, remain indeed self-similar inside the plume while it meanders around its axis. Thus, unless otherwise specified, the conditional averages used below will be estimated only for condition k_1 (denoted hereinafter by $\langle \varphi_j \rangle|_k$) associated with the plume centreline position within a circle of $Delta = 5$ centred on the injector. The ensemble averages of all the data, under the ergodic hypothesis, are equivalent to the global time average and will be denoted by $\overline{\varphi_j}$.

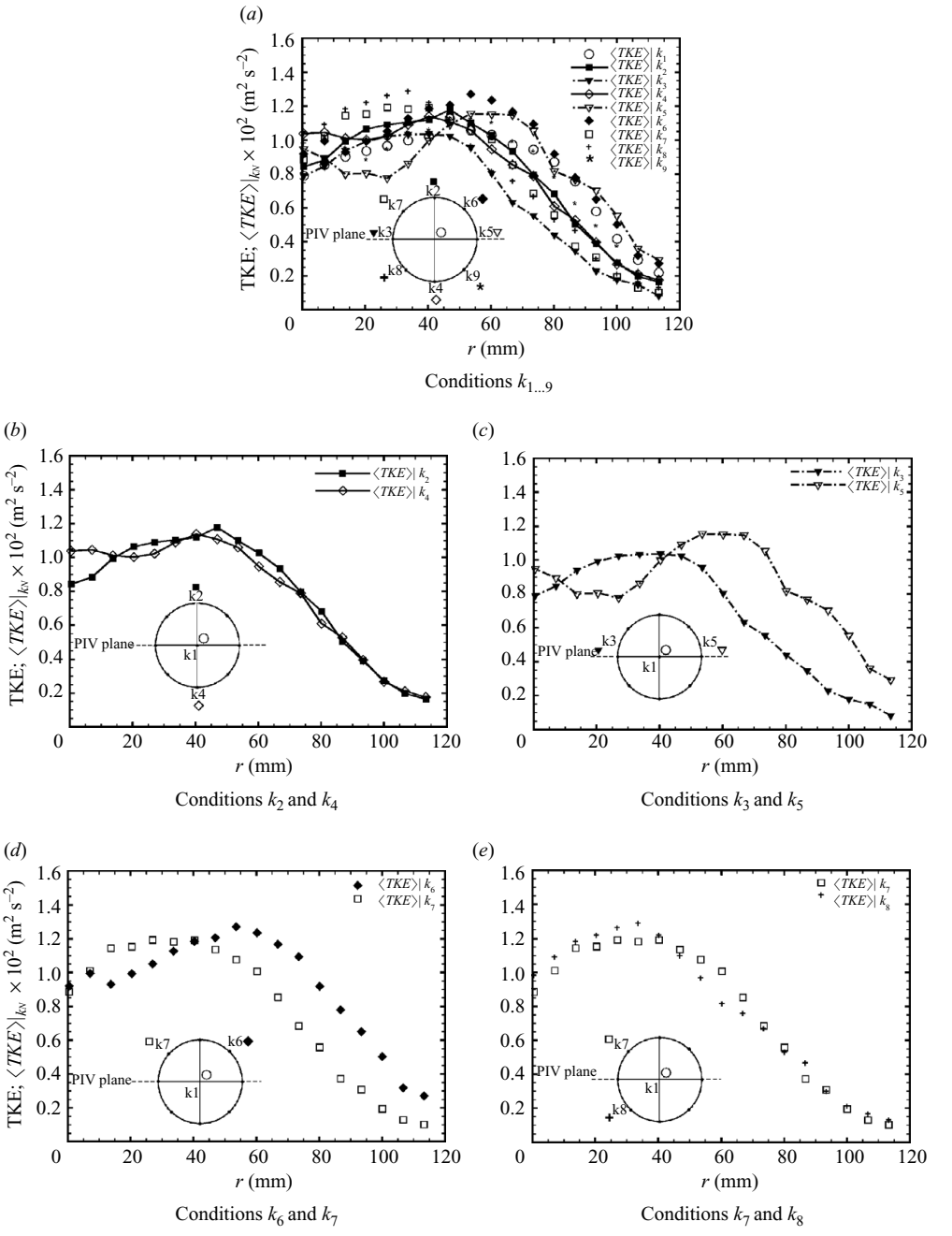

FIGURE 18. Comparisons of the global-time-average TKE and conditional average turbulent kinetic energy $\langle TKE\rangle|_{k_n}$, obtained for various conditions (always $Delta = 5$ mm), for the gas flow rate of 15 NL min^{-1}, at the 700 mm elevation. The points k are on a circle having a radius of 10 mm centred on the injector centreline.

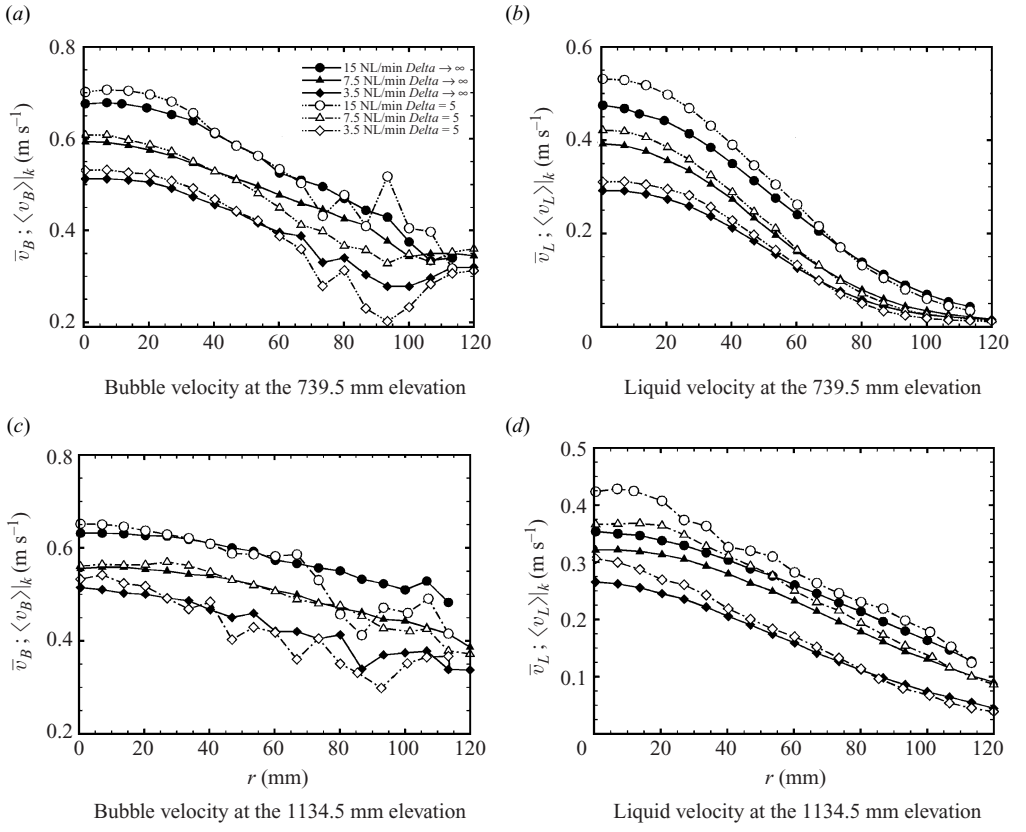

FIGURE 19. Global time ($Delta \to \infty$) and conditional ($Delta = 5$ mm) average bubble and liquid velocity profiles for three gas flow rates, at the 739.5 and 1134 mm elevations.

7.2. *Conditional and ensemble-averaged velocities*

Conditional (position k_1, $Delta = 5$ mm) and global time ($Delta \to \infty$) averages of the bubble velocity are shown in figures 19(a, c) for different flow rates, at two elevations. The differences do not exceed 5 % at the centreline of the plume and may reach 10 % at the periphery where the scatter is greater due to the small number of samples, as already noted.

For the liquid phase, the statistical reliability of the averages at the plume edge is good. In figure 19(b, d), the differences of the conditional and ensemble averages of the liquid velocity are larger than those of the bubble velocity, reaching more than 10 % at the centreline for the highest gas flow rate. This can be explained by the fact that the liquid velocity across the plume has a much steeper profile than the bubble velocity. Thus, the influence of meandering is weaker for the gas velocity.

7.3. *Conditional and ensemble averages of the second-order moments of the velocity*

The influence of large structures on the overall flow becomes substantial for the second-order moments of the velocity field, in particular for the Reynolds stresses and the turbulent kinetic energy.

The three Reynolds stress terms are plotted in figure 20 for three gas flow rates at about half the total water immersion depth. The peaks, for both the conditional and the global average distributions, are roughly located at the same position ($r = 50$ mm),

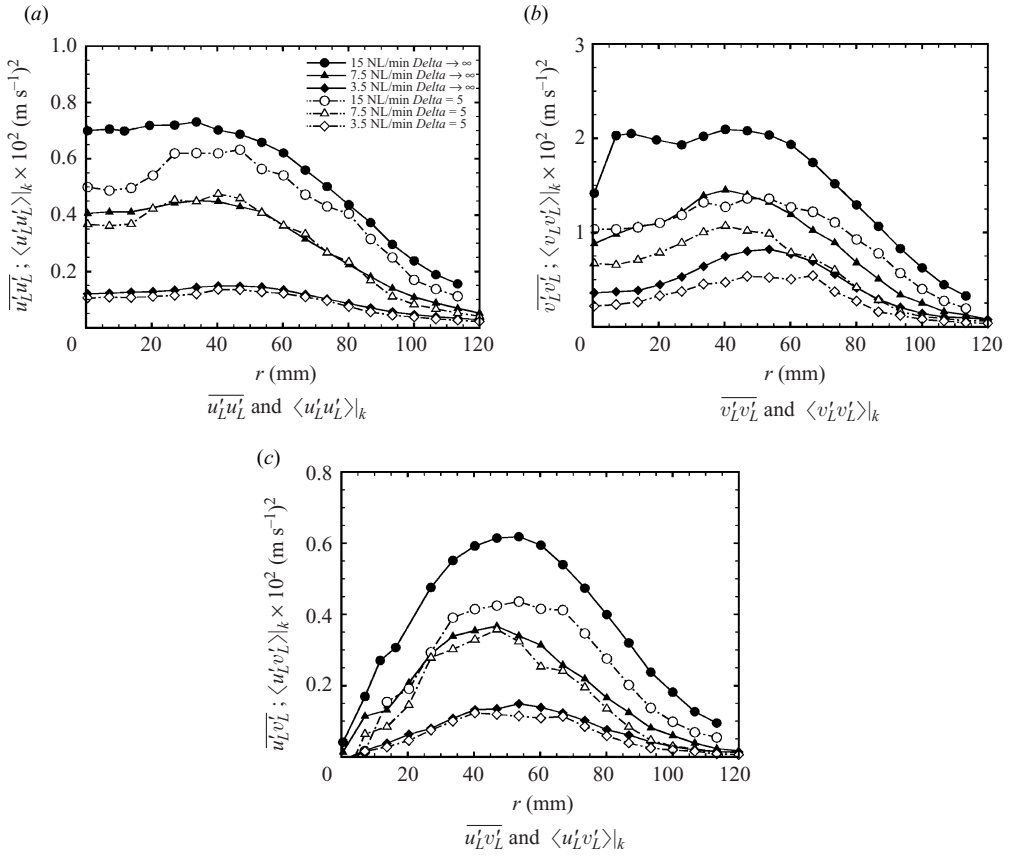

FIGURE 20. Global time ($Delta \to \infty$) and conditional ($Delta = 5$ mm) average Reynolds stress term profiles of the liquid phase for the four gas flow rates at the 739.5 mm elevation.

where the Reynolds stresses show conspicuous differences, especially at the high flow rates. The effect of LS motions is clearly more pronounced for the vertical normal stress distributions (figure 20*b*), where the differences between global and conditional averages increase steadily with flow rate (about 40–50 % at 15 NL min^{-1}). The radial normal Reynolds shear stresses, figure 20(*a*) exhibit a similar influence of the filtering but, the differences are important only at high flow rates.

As expected, and also as reported in Part A of this work, close to the injector, TKE and $\langle TKE \rangle|_k$ are not very different, especially at low flow rates. Otherwise, further downstream ($Y/D_{inj} = 4.8$) the contribution of the large structures becomes significant and increases with flow rate, as shown in figure 21(*a*). The effect of the LS structures, however, reaches a saturation for $Y/D_{inj} = 7.6$, where the difference between TKE and $\langle TKE \rangle|_k$ starts vanishing, as shown in figure 21(*b*). This saturation effect is consistent with the observed trend of the oscillation of the plume centreline reported in figure 8.

8. Conditional averages according to the bubble plume diameter

Visual observations of the bubble plume dynamics have revealed a complex oscillatory behaviour of its structure. The LS motions consist of coupled phenomena, i.e. a three-dimensional meandering of the plume around its axis and superimposed fluctuations of its horizontal cross-section. To detect their respective contributions to

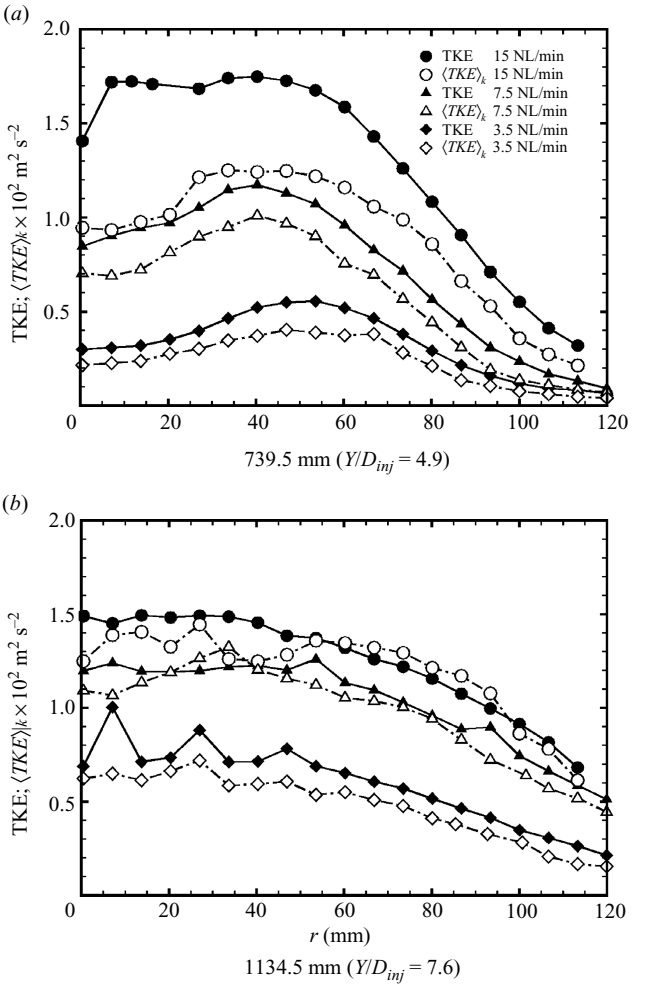

FIGURE 21. Global- and conditional- average kinetic turbulence profiles, TKE and $\langle TKE\rangle|_k$ of the liquid phase for all four gas flow rates, at the 739.5 and 1134.5 mm elevations.

the time-averaged quantities is not a trivial task. In this section, we shall address now the additional influence of the plume diameter fluctuation.

Histograms of observed distributions of bubble plume diameters are given in figure 22 for two different elevations. The plotted *occurrence* represents the number of collected PIV velocity fields associated with a certain range of plume diameters (about 5 mm bins). The plume diameter considered here is again an average over the height of the PIV window of about 210 mm.

To partly remove the first, coherent effect due to plume meandering and focus only on plume diameter fluctuations, the conditional averages, according to plume diameter denoted here by $\langle\rangle|_{D_e}$, were computed over vector fields related to a maximum displacement of the plume centreline from the injector centreline of 15 mm, ($Delta = 15$ mm), re-centring the instantaneous vector fields on the injector centreline before averaging (in a Lagrangian fashion). It was not possible to further restrict *Delta* (as was done in § 7), because the available number of vector fields would have been extremely reduced. These ensemble averages are denoted by '$Delta = 15$' in the following figures. The re-centring corrects the data adequately for displacement within

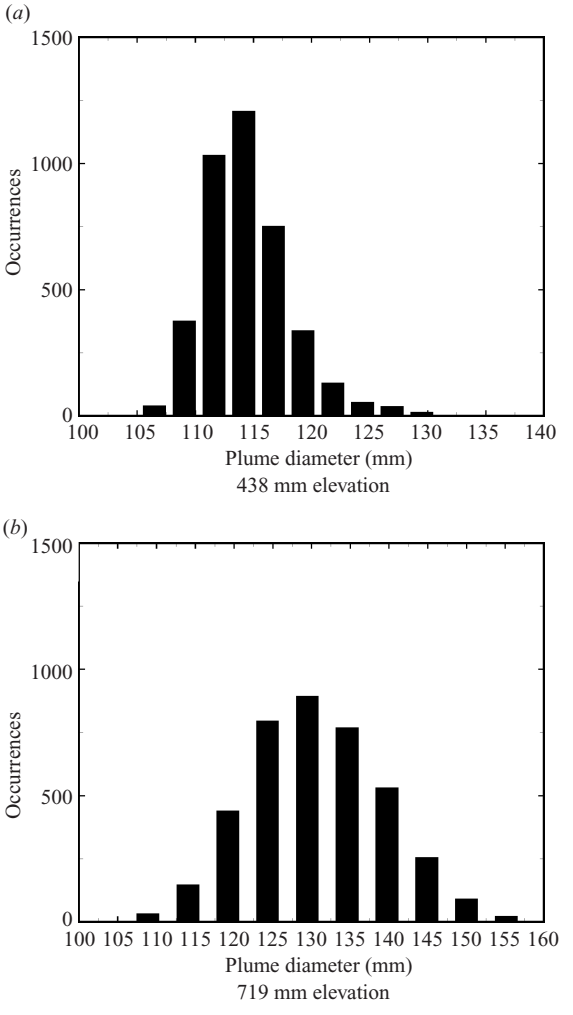

FIGURE 22. Histograms of the plume diameter occurrences at the gas flow rate of $15\,\mathrm{NL\,min^{-1}}$.

the PIV plane (as shown in figure 18); the effect of the displacement away from the PIV plane remains.

As a practical and reasonable approach to further conditional averaging, the bubble plume diameters were divided into five groups related to five bubble plume diameters, $D_e \pm 10\,\%$, such that a sufficient number of PIV vector fields was available for statistically reliable conditional averaging. However, the frequency of occurrences for the smallest and largest selected bubble plume diameter bins was sometimes quite low (points on the histogram tails), so that the statistical accuracy may be debatable. The results of these investigations are discussed in the following sections.

8.1. *Bubble, liquid and relative velocities*

It was previously shown that, very close to the injector, the weak meandering of the bubble plume has no effect on the global time averages. For this reason, the influence of fluctuations of the horizontal cross-section can be well isolated. At very low elevations, the horizontal cross-section of the bubble plume was fluctuating

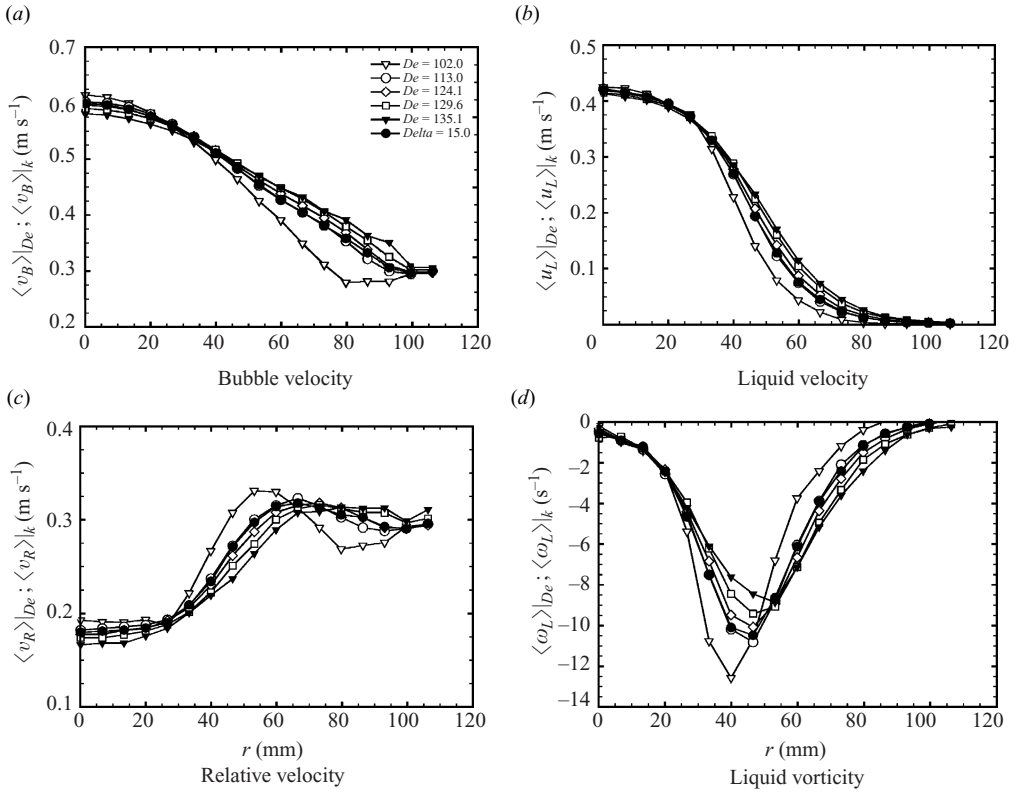

FIGURE 23. Conditional average (according to plume diameter *De*) bubble and liquid velocities, relative velocities, and vorticity at the 438 mm elevation for the gas flow rate of 15 NL min^{-1}.

weakly, but at an elevation of about 300 mm, some differences between the conditional averages could already be detected.

Conditional averages of the dispersed-phase velocity at the 438 mm elevation are displayed in figure 23(*a*) and show that, as expected, smaller bubble plume diameters are associated with narrower velocity profiles, while larger bubble plume diameters show instead broader velocity profiles with slightly lower central values. It is not surprising that, for example, for the case of plume diameter $D_e = 113$ mm (± 11.3 mm) $\langle v_B \rangle|_{D_e}$ shows a span of about 190 mm. This can be explained by several factors: The bubble diameter used to select the velocity fields is an average plume diameter over the entire vertical PIV field of view; at some elevations it can be smaller or larger. The bubble plume diameter is obtained by image analysis from the video recordings, possibly ignoring some bubbles outside the core of the plume, which contribute, however, to the PIV sample. Finally, near the plume edge some points may be averages over only a few velocity vectors.

The conditional-average liquid velocities presented in figure 23(*b*), show a behaviour similar to that of the dispersed phase. The profiles associated with small diameters are narrower as well, with slightly lower centreline velocity. Moreover, the profiles have an accentuated slope, which is also reflected in the vorticity profiles shown in figure 23(*d*), where a radial displacement of the mixing layer occurs when an expansion or a contraction of the bubble plume takes place. This correlation between instantaneous plume diameter and instantaneous liquid- and bubble-velocity fields reveals the

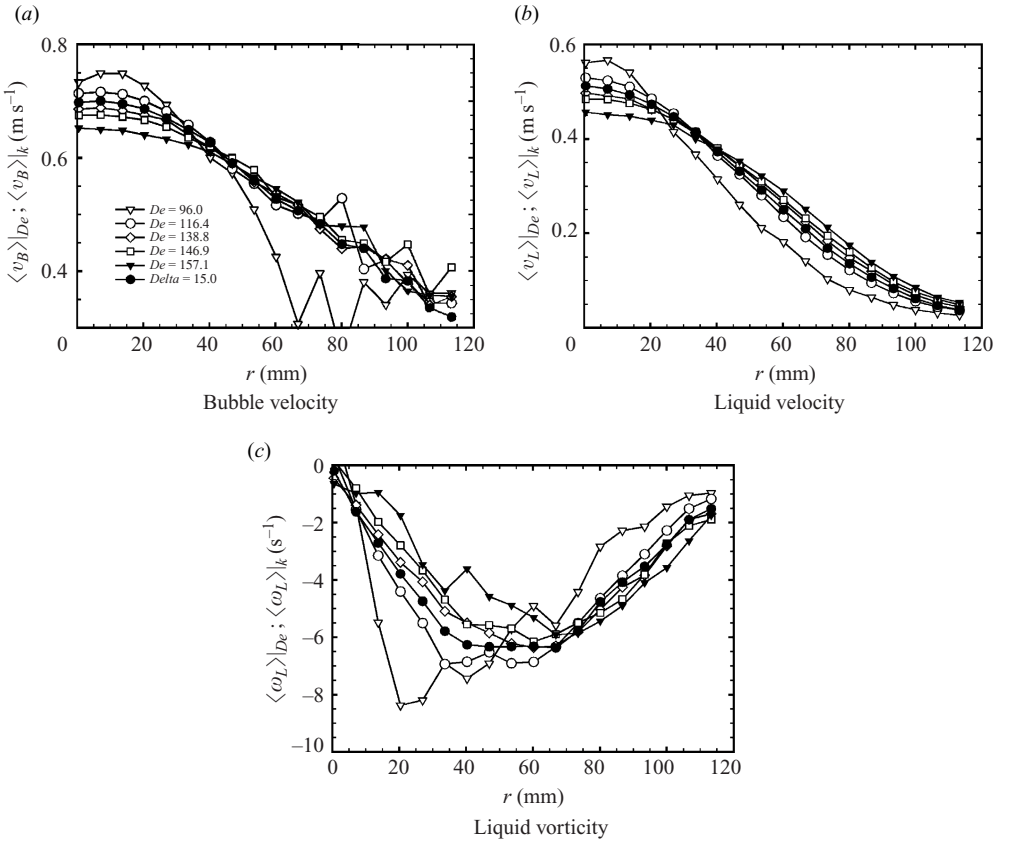

FIGURE 24. Conditional average (according to plume diameter D_e) bubble and liquid velocities and vorticity at the 739 mm elevation for the gas flow rate of 15 NL min^{-1}.

instantaneous redistribution of phase velocities according to the instantaneous bubble plume diameter; the velocity profile tends to be self similar within its instantaneous diameter. This conclusion, arrived at thanks to the conditional-average approach, could not be derived from the instantaneous PIV frames because of the noise present in the instantaneous phase-velocity profiles.

The conditional-average relative velocities reported in figure 23(*c*) are also strongly influenced by the instantaneous bubble plume diameter. As already observed in Part A, § 5.1, the relative velocity exhibits a radial evolution with a steep gradient corresponding to the zone of large gradient of the bubble and liquid velocity profiles. This was explained as an effect of radial bubble migration producing a momentum exchange between high- and low-velocity zones. In the same way, the steeper relative velocity curves correspond to the steeper bubble and liquid velocity profiles present in the small bubble plume diameters as again the bubble migration from high- to low-velocity zones (and vice versa) has a stronger impact on the relative velocity in the presence of steep gradients of the phase velocities. Moreover, the fluctuation of the bubble plume diameter, coupled with the observed wavy motion of its edge, may act as a propulsion mechanism for the migration, lifting and dragging of bubbles from the periphery to the plume centre and vice versa.

Further away from the injector, at the elevation of 739 mm (figure 24), the trends previously described become more evident but the profiles look noisy now. Indeed,

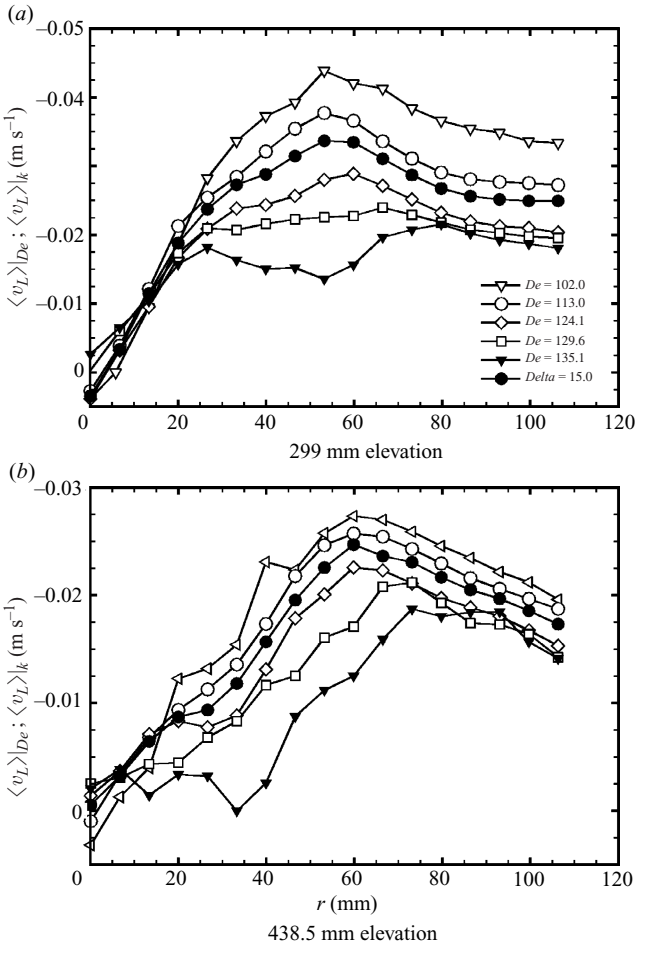

FIGURE 25. Conditional average (according to plume diameter *De*) horizontal liquid velocity component for the gas flow rate of 15 NL min^{-1} at two elevations.

at this elevation, plume meandering was stronger, and thus the constraint $Delta = 15$ had a stronger filtering effect; the conditional averages, especially for the smallest and largest diameters, contain fewer vector fields (about 100), making the profiles scatter. For the liquid and bubble velocities shown in figures 24(*a*, *b*), the centreline velocity spread for different bubble plume diameters can reach 20 %. Such fluctuations, which are related to the plume diameter variation, could not be distinguished from the random or incoherent fluctuations when only global time-averages were performed and random fluctuations were overestimated.

In figure 25 the conditional average horizontal liquid velocity component is plotted for the 299 and 438 mm elevations. This component is always negative, because of the entrainment of the liquid producing the spreading of the vertical velocity profile. The entrainment varies with the instantaneous bubble plume diameter, showing a higher value with decreasing diameter: smaller plume cross-sections produce stronger entrainment then larger ones. This contradicts most of the models or empirical correlations based on time averaged quantities that predict larger entrainment for larger plume diameters. In time-average terms, Milgram (1983) reported the

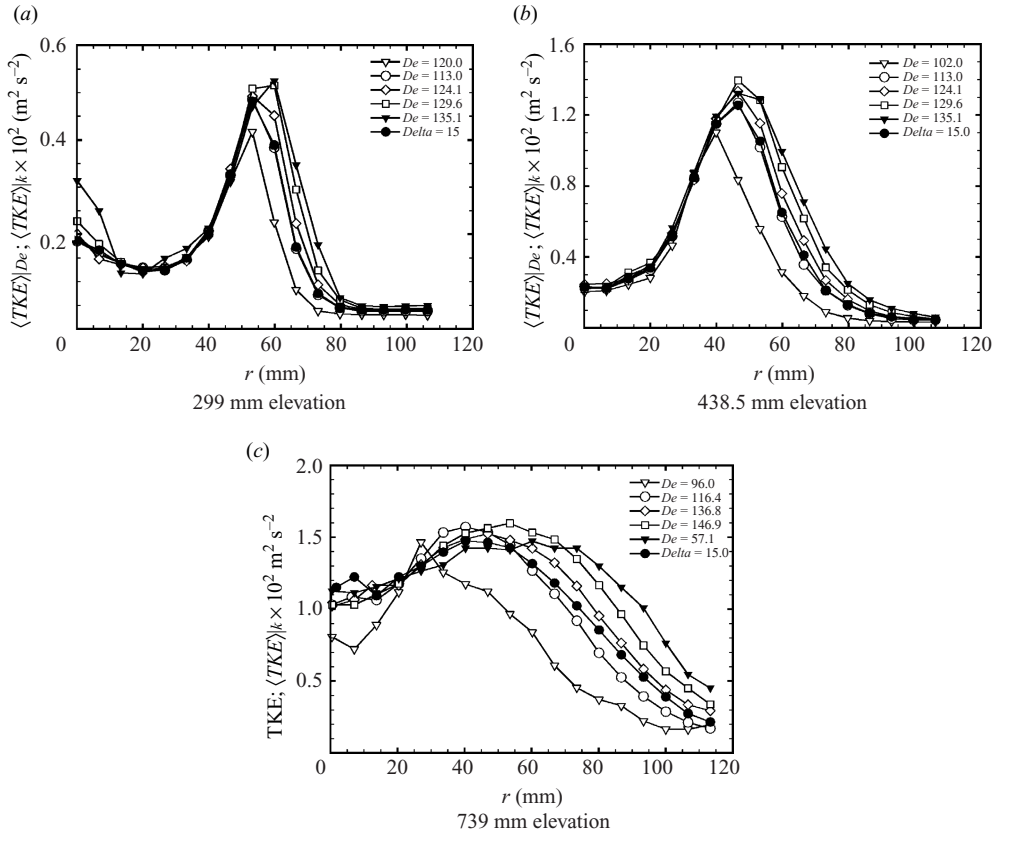

FIGURE 26. Conditional averages according to the diameter range, $\langle TKE\rangle|_{De}$, and average of all the data for $Delta = 15$ mm, $\langle TKE\rangle|_k$, of the turbulent kinetic energy distributions for the gas flow rate of 15 NL min^{-1}.

entrainment coefficient increasing with the characteristic bubble mixing length which increases with the bubble plume diameter. On the other hand, again Milgram (1983) recognized the undulation and folding of the bubble plume interface as an important propulsion mechanism of the entrainment process. The three-dimensional reconstruction of the bubble plume structure (figure 5) shows large instabilities of the gas region that is experiencing plume diameter fluctuations. These instabilities trigger 'entrainment eddies' which instantaneously increase the entrainment and therefore the inward-flow velocity. Due to the large scatter of the instantaneous liquid velocity, this phenomenon can only be observed by making conditional averages.

Farther away from the injector, at the elevation of 700 mm, the trend is still the same, although attenuated, probably because the plume meandering could not be fully isolated by the limited $Delta = 15$ mm filtering.

8.2. *Turbulence statistics*

Conditional-average kinetic energy profiles of turbulence are shown in figure 26. Near the plume centre, the turbulent kinetic energy does not show obvious changes with plume diameter, in contrast to the situation at the plume periphery. The peak is shifted towards the centre and narrow profiles are visible for smaller plume diameters, as expected. Moreover, as is evident in particular at the 438-mm-elevation, the larger

plume diameters contribute more to the turbulent kinetic energy than the smaller ones, as the distributions become taller and broader. At the highest elevation, this effect becomes even stronger (see figure 26*c*).

9. Conclusions

The results of an intensive experimental investigation of a bubble plume exhibiting three-dimensional, unstable motions were presented. A two-camera PIV system was used to measure simultaneously the velocity fields of the two phases. An additional, two-video-camera recording system was installed to study the plume structure dynamics, including the instantaneous plume centreline position and its equivalent circular-plume diameter. Conditional averages were defined using these two parameters to characterize the state of the plume, and then used to separate the small-scale fluctuations of the flow from its large-scale motions, namely the plume meandering and the instantaneous cross-sectional area fluctuations. These two classes of events can be identified as individual energetic events in the sense of Farge (1992), in that they are coherent, non-periodic, in non-equilibrium and uncorrelated with the sub-scale motions, ranging in size from that of typical swarms of bubbles to the Kolmogorov dissipative scales.

With the two-PIV-camera setup, radial profile measurements made near the injector where the plume was relatively stable, showed, near the periphery of the plume, differences between the true time-average relative velocities and the difference of the averaged phase velocities (vertical components). The complex, non-monotonic, radial variations of the true relative velocity and its evolution downstream were explained by the effects of passing vortices created near the injector and vanishing downstream, and by the fact that the bubbles do not reach an equilibrium velocity as they migrate radially, exchanging momentum between high- and low-velocity regions.

Void fraction measurements show a contraction of the plume near the injector, promoting flow acceleration while affecting the distribution of the stresses. In this contraction area, the relative velocities exhibit a sharper profile at the plume edge. This finding was explained by bubble migration between the high- and low-momentum flow areas.

The observations of the plume far downstream have shown little instantaneous spreading of the plume diameter although the globally time averaged data suggest the opposite. The velocity and void fraction profiles along the instantaneous plume cross-section tend to remain self-similar.

The spectral analysis of the plume axial position revealed a continuous precession of the plume (main mode) with a frequency scaling with flow rate, as already observed in earlier experiments (Milgram 1983; Rensen & Roig 2001; Simiano *et al.* 2006). Plume precession is just one part of the more complex plume meandering, featuring more energetic contributions from the instantaneous interaction of the plume with the rising liquid vortices created at its edge.

Away from the injector where the plume is unstable, a conditional-average approach based on the assumption of triple flow decomposition was used to identify the contribution of the large-scale motion of the plume. This contribution was separated by considering and filtering out the effects of plume meandering and the variation of the plume equivalent diameter. Conditional averaging based on the position of the plume centreline alone revealed preservation of plume similarity, independently from its instantaneous position; similarity was present in the average velocity profiles

and more substantially in the profiles of the turbulent quantities. The influence of the plume diameter variations on the mean quantities was examined in a second set of conditional averages where the plume position was confined to a radius of 15 mm around the injector centreline. The velocity fields of both phases were found to correlate with the instantaneous plume diameter, revealing an instantaneous redistribution of the phase velocities towards similarity. Further, the liquid and bubble centreline velocities were found to vary with the instantaneous bubble plume diameter. An important finding is that plume meandering does not affect the instantaneous turbulent kinetic energy distribution in the plume, suggesting again that large scales and sub-scales are not correlated. These interesting observations could not have been realized without the conditional-averaging approach introduced here. Local entrainment effects appeared to be strongly dependent on the instantaneous plume diameter, reducing in strength for larger plume diameters. This finding, which contradicts the opposite trend obtained from classically time averaged quantities, shows that the dynamic undulation and folding of the bubble plume interface is an important mechanism for the entrainment process. The instabilities observed for small bubble plume diameters tend to trigger 'entrainment eddies', which instantaneously promote entrainment and thus the inward-flow motion.

Sub-scale turbulent properties of the flow were estimated, revealing an anisotropic transport mechanism with strong shear-induced characteristics. The large-scales induced by plume meandering were found to exert a minor effect on the global kinetic energy and the Reynolds stresses. In contrast, the large-scale motions associated with plume contraction, reflected in the variation of the plume diameter, were found to exert a substantial effect on the kinetic energy and individual components of the Reynolds stress tensor; their impact depends, however, on the gas flow rate and distance from the injector.

From a modelling point of view, it is unlikely that any class of RANS approach would provide a faithful picture of what really happens instantaneously in such flows, all the more if applied at steady state. RANS models may solely address the low-frequency, shear-induced production and dissipation of the kinetic energy. Three-dimensional oscillating bubbly flows require a simulation strategy such as LES to resolve the large-scale motions, including plume meandering, plume diameter fluctuations (e.g. Lakehal, Smith & Milelli 2002), contraction, etc.

The data and findings collected in this paper constitute now a new basis and a new challenge for modelling the phenomena and testing closure laws under real, time-dependent flow conditions, rather than simply matching averages.

The authors gratefully acknowledge support from the Emil Berthele Fonds (ETH Zurich). The experiments were performed at the Thermal-Hydraulics Laboratory of the Paul Scherrer Institut (PSI). The authors are grateful to Professor Véronique Roig for advice on the experiments conducted, and to Dr Beat Sigg for his perusal of and contributions to this paper and thoughtful suggestions. The numerous technical contributions of Max Fehlmann, the project management of Dr François de Cachard and the expertise of Dr Robert Zboray regarding the optical probes are also gratefully acknowledged.

Appendix: The average of the instantaneous relative velocity

The PIV measurements provide the liquid and bubble velocities v_B and v_L, respectively, by cross-correlation with the space and time averaging inherent to this technique. The velocities are estimated in an IR which instantaneously (in reality

quasi-instantaneously, since the PIV measurement needs two distinct pulses) can be partially occupied by liquid and/or gas. For each PIV shot, the part of the IR which is occupied by the gas appears as a black spot in the liquid-PIV picture and it does not contribute to the correlation. The same happens to the zone occupied by the liquid in the bubble-PIV pictures. Thus, each k-phase PIV measurement (where k is L for liquid and B for gas) is estimated only in the region properly occupied by the phase considered and the measurement ends up being weighed by the respective characteristic function of that phase defined, at the point x, as:

$$\chi^k = \begin{cases} 1 \to x \in k \\ 0 \to x \notin k \end{cases}. \tag{A 1}$$

The quasi-instantaneous bubble and liquid velocities can be generally written as:

$$\begin{aligned} v_B &= \frac{\langle v_B \chi^B \rangle}{\langle \chi^B \rangle}, \\ v_L &= \frac{\langle v_B \chi^L \rangle}{\langle \chi^L \rangle}, \end{aligned} \tag{A 2}$$

where the operator '$\langle\rangle$' denotes, in this context, the inherent cross-correlation averaging of the PIV technique where the phase velocities and the χ^k are averaged over the volume defined by the IR and the laser beam thickness as width. One can then compute the quasi-instantaneous relative velocity as $v_R = v_B - v_L$.

When time averages of the phase velocities are computed, another characteristic function η_k should be defined for each phase k to ensure that it is present and a valid instantaneous measurement has been obtained for the samples used to compute the averages:

$$\begin{aligned} \overline{v_B} &= \frac{\overline{v_B \eta_B}}{\overline{\eta_B}}, \\ \overline{v_L} &= \frac{\overline{v_L \eta_L}}{\overline{\eta_L}}. \end{aligned} \tag{A 3}$$

The two 'experimental' characteristic functions η_L and η_B are equal to 1 when phase k is present in the IR and equal to 0 otherwise. The true mean relative velocity is then computed as:

$$\overline{v_R} = \frac{\overline{(v_B - v_L)\eta_B \eta_L}}{\overline{\eta_B \eta_L}} \neq \frac{\overline{v_B \eta_B}}{\overline{\eta_B}} - \frac{\overline{v_L \eta_L}}{\overline{\eta_L}}. \tag{A 4}$$

This inequality clearly proves that the properly averaged relative velocity may differ from the difference of the averages. The true mean relative velocity contains the product of the characteristic functions η_L and η_B, which ensures that the instantaneous relative velocity is considered for the average only when both phases coexist in the control volume.

REFERENCES

van den Berg, T. H., Luther, S., Mazzitelli, M., Rensen, J. M., Toschi, F. & Lohse, D. 2006 Turbulent bubbly flow. *J. Turbul.* **7** (14), 1–12.

Cartellier, A. 1990 Optical probes for local void fraction measurements: characterization of performance. *Rev. Sci. Instrum.* **61** (2), 871–874.

Cartellier, A. & Achard, J. L. 1991 Local phase detection probes in fluid/fluid two-phase flow. *Rev. Sci. Instrum.* **62** (2), 279–303.

Castello-Branco, M. A. S. C. & Schwerdtfeger, K. 1994 Large-scale measurements of the physical characteristics of round vertical bubble plumes in liquids. *Metall. Trans.* B **25B**, 359–371.

Delnoj, E., Westerweel, J., Deen, N. G., Kuipers, J. A. M. & van Swaaij, W. P. M. 1999 Ensemble correlation PIV applied to bubble plumes rising in a bubble column. *Chem. Engng Sci.* **54**, 5159–5171.

Fannelop, T. K., Hirschberg, S. & Kuffer, J. 1991 Surface current and recirculating cells generated by bubble curtains and jets. *J. Fluid Mech.* **229**, 629–657.

Farge, M. 1992 Wavelet transforms and their applications to turbulence. *Annu. Rev. Fluid Mech.* **24**, 395–457.

Grevet, J. H., Szekely, J. & El-Kaddahn, N. 1981 An experimental and theoretical study of gas bubble driven circulation systems. *Intl J. Heat Mass Transfer* **25** (4), 487–497.

Gross, R. W. & Kuhlman, J. M. 1992 Three-component velocity measurements in a turbulent recirculating bubble-driven liquid flow. *Intl J. Multiph. Flow* **18** (3), 413–421.

Hassan, Y. A., Blanchat, T. K., Seeley, Jr., C. H. & Canaan, R. E. 1992 Simultaneous velocity measurements of both components of a two-phase flow using particle image velocimetry. *Intl J. Multiph. Flow* **18** (3), 371–395.

Hinze, J. O. 1959 *Turbulence*. Mcgraw–Hill.

Iguchi, M., Shinkawa, M., Nakamura, H. & Morita, Z. 1995 Mean velocity and turbulence of water flow in a cylindrical vessel agitated by bottom air injection. *ISIJ Intl* **35** (12), 1431–1437.

Iguchi, M., Takeuchi, H. & Morita, Z. 1991 The flow field in air-water vertical bubbling jets in a cylindrical vessel. *ISIJ Intl* **31** (3), 246–253.

Ishii, M. & Zuber, N. 1979 Drag coefficient and relative velocity in bubbly, droplet or particulate flows. *AIChE J.* **25**, 843–855.

Johansen, S. T., Robertson, D. G. C., Woje, K. & Engh, T. A. 1988 Fluid dynamics in bubble stirred ladles. Part I. Experiments. *Metall. Trans.* B **19B**, 745–754.

Kobus, H. E. 1968 Analysis of the flow induced by air-bubble system. In *Proceedings of the*11*th Conference on Coastal Engineering*, London, England, vol. 2, pp. 1016–1031.

Kubasch, J. H. 2001 Bubble hydrodynamics in large pools. Doctoral dissertation, ETH No. 14398, Zurich, Switzerland.

Kuwagi, K & Ozoe, H. 1999 Three-dimensional oscillation of bubbly flow in a vertical cylinder. *Intl J. Multiph. Flow* **25**, 175–182.

Lakehal, D., Smith, B. L. & Milelli, M. 2002 Large-eddy simulation of bubbly turbulent shear flows. *J. Turbul.* **3**, 895–900.

Mazzitelli, I. M. & Lohse, D. 2003 The effect of microbubbles on developed turbulence. *Phys. Fluids* **15** (1), L5–L8.

Milgram, J. H. 1983 Mean flow in round bubble plumes. *J. Fluid Mech.* **133**, 345–376.

Rensen, J., Luther, S. & Lohse, D. 2005 The effect of bubbles on developed turbulence. *J. Fluid Mech.* **538**, 153–187.

Rensen, J. & Roig, V. 2001 Experimental study of the unsteady structure of a confined bubble plume. *Intl J. Multiph. Flow* **27**, 1431–1449.

Rightley, P. M. & Lasheras, J. C. 2000 Bubble dispersion and interphase coupling in a free-shear flow. *J. Fluid Mech.* **412**, 21–59.

Simiano, M. 2005 Experimental investigation of large-scale three dimensional bubble plume dynamics. Doctoral dissertation, ETH No. 16220, Zurich, Switzerland.

Simiano, M., Zboray, R., de Cachard, F., Lakehal, D. & Yadigaroglu, G. 2006 Comprehensive experimental investigation of the hydrodynamics of large-scale, three-dimensional bubble plumes. *Intl J. Multiph. Flow* **18** (32), 1160–1181.

Tacke, K. H., Schubert, H. G., Weber, D. J. & Schwerdtfeger, K. 1985 Characteristic of round vertical gas bubble jets. *Metall. Trans.* B **16B**, 263–275.

van Wijngaarden, L. 1998 On pseudo turbulence. *Theor. Comput. Fluid Dyn.* **10**, 449–458.

Wu, Q. & Ishii, M. 1999 Sensitivity study on double-sensor conductivity probe for the measurement of interfacial area concentration in bubbly flow. *Intl J. Multiph. Flow* **25**, 155–173.

Zenit, R., Koch, D. L. & Sangani, A. S. 2001 Measurements of the average properties of a suspension of bubbles rising in a vertical channel. *J. Fluid Mech.* **429**, 307–342.

Zuber, N. & Findley, J. A. 1965 Average volumetric concentration in two-phase flow system. *ASME J. Heat Transfer* **87**, 453–465.